Flow-acoustic resonance in deep and inclined cavities

You Wei Ho[1*] and Jae Wook Kim[2]
[1] *Institute of Sound & Vibration Research, University of Southampton, Southampton, SO17 1BJ, United Kingdom*
[2] *Aeronautics & Astronautics, University of Southampton, Southampton, SO17 1BJ, United Kingdom*
(Dated: June 27, 2025)

This paper presents numerical investigations of flow-acoustic resonances in deep and inclined cavities using wall-resolved large-eddy simulations. The study is based on a fixed aspect ratio of $D/L = 2.632$, subjected to two Mach numbers of 0.2 and 0.3 (with the focus on the latter) at three different angles of inclination ($\alpha = 30°$, $60°$, and $90°$). Fully turbulent boundary layers generated from independent precursor simulations are employed upstream of the cavities. The simulation results show significant differences in aeroacoustic response between inclined and orthogonal cavities, particularly at $M_\infty = 0.3$, where the inclined cavities exhibit stronger resonances (by more than a 20 dB) at a lower peak frequency ($St = 0.276$) compared to that of the orthogonal cavity, which occurred at $St = 0.849$. Acoustic modal analysis identifies these frequencies as the 1st and 2nd eigenmodes, respectively. Further analysis shows that the disparity in mode selection between the orthogonal and inclined cavities is linked with the hydrodynamic modes (vortex dynamics) that pair with the acoustic modes. In the orthogonal cavity, a 2nd hydrodynamic mode prevailed where two relatively small vortices were travelling across the cavity opening simultaneously. In the inclined cavities, however, a single large-scale roll-up vortex, a 1st hydrodynamics mode, is generated in relation with strong Kelvin-Helmholtz instability in the shear layer. More importantly, the vortex spends a substantial amount of its lifetime growing in size without travelling downstream rapidly. This results in a longer crossing time per cycle which correlates with the 1st acoustic eigenmode frequency ($St = 0.276$). In addition, an aeroacoustic resolvent analysis indicates that inclined cavities amplify acoustic responses more effectively and exhibit weaker source-sink cancellations than the orthogonal cavity. These mechanisms are identified as the primary contributors to the enhanced aeroacoustic responses in the inclined cavities. Finally, it is proposed that the ratio between acoustic particle displacement and momentum thicknesses may be used as a criterion to predict the onset of deep cavity resonance with the distinctive vortex dynamics identified in this paper.

I. INTRODUCTION

Flow-acoustic resonances driven by aeroacoustic instabilities in deep cavity flows produce high-intensity pressure waves at discrete frequencies, leading to detrimental effects such as noise pollution and structural fatigue in various engineering applications. These include safety valves [1, 2], closed side-branches in gas transport systems [3, 4], turbomachinery [5, 6], and riverine environments [7]. The origin of these resonances lies in the complex interaction between hydrodynamic instabilities and resonant acoustic fields [3, 8]. When airflow passes over a deep cavity under specific conditions, it can trigger self-sustained oscillations that couple with a depthwise acoustic mode, generating intense aerodynamic noise. In this process, acoustic resonance acts as the primary feedback mechanism, amplifying oscillations and inducing flow tone lock-ins [9]. This phenomenon is fundamentally different from oscillations in shallow cavities, which are predominantly governed by the Rossiter feedback mechanism driven by upstream acoustic feedback [10, 11]. Therefore, a better understanding of the distinct physical mechanisms underlying deep cavity oscillations is essential for mitigating their adverse effects in engineering applications.

The aeroacoustics of deep cavity flows have been extensively studied in the scientific literature. Seminal works by [10, 12–14] established that deep cavity flows generate intense acoustic responses near depthwise acoustic modes. Rockwell and Naudascher [15] characterized this phenomenon as fluid resonant oscillation, driven by the interaction between shear-layer instabilities and depthwise acoustic resonances. Their research revealed that these oscillations originate from initial shear-layer instabilities near the upstream separation corner. As these instabilities propagate downstream, they interact with the cavity's trailing edge and generate acoustic standing waves. This resonant acoustic field, in turn, induces velocity perturbations that reinforce shear-layer instabilities, thereby sustaining a closed feedback loop. In deep cavity systems, this loop is particularly pronounced due to their inherent susceptibility to minimally radiating depthwise acoustic modes [16]. As a result, these acoustic resonances can further amplify shear-layer instabilities, giving rise to highly coherent vortex structures frequently observed in deep cavity flows [17–20].

* Corresponding author: ywh1u18@soton.ac.uk

The presence of coherent vortices implies that the phenomenon of flow-acoustic resonances in deep cavities typically occurs within specific Strouhal number ranges, each corresponding to a distinct hydrodynamic mode of the flow field. These modes are characterized by the number of convecting vortex structures across the cavity opening that satisfy the requisite streamwise phase criterion [21–23]. Among these, flow-acoustic resonances driven by the 1st hydrodynamic mode are well-documented for generating the most intense acoustic responses, predominantly occurring at a Strouhal number of approximately $St \approx 0.4$ [18]. In contrast, higher hydrodynamic modes produce weaker resonances at Strouhal numbers exceeding $St \approx 0.8$ [9, 18]. Recent experimental investigations on closed side-branches have revealed an additional category of flow-acoustic resonance at a lower Strouhal number, $St \approx 0.27$. This resonance is distinguished by exceptionally strong acoustic responses, surpassing the dynamic pressure of the flow [8, 9, 24–26]. Moreover, within this regime, the resonant acoustic field exerts a significant influence on the coherence and trajectory of vortex structures. Peters [8] observed that under these conditions, the amplification of instabilities and the intensification of shear-layer oscillations lead to highly nonlinear states, making precise characterization of the fluid resonant mechanism increasingly complex. However, despite substantial empirical evidence, a detailed quantitative analysis of the physical mechanisms governing these pronounced flow-acoustic resonances at $St \approx 0.27$ remains an unresolved challenge.

Recent advances in modal analysis techniques including global linear stability analysis and receptivity analysis have become essential for investigating long-term flow instabilities and revealing the mechanisms behind instability in various fluid-flow systems [27–37]. Direct global and adjoint modes obtained from these methods offer critical insights into structural sensitivity within flow fields [28, 32, 35, 38]. Additionally, non-modal approaches, such as resolvent analysis, initially introduced by Trefethen et al. [39] and later extended to turbulent mean flows by McKeon et al. [40] provide a foundational framework for studying energy amplification and the structural response to perturbations across various frequencies. These methods have been applied to both shallow and deep cavity flows, yielding valuable insights into their underlying dynamics [41–44]. However, the application of resolvent analysis to examine flow-acoustic resonances in deep and inclined cavity flows remains unexplored. In addition, to our knowledge, this approach has not yet been used to identify the optimal forcing, response, and amplification mechanisms of acoustic perturbations that trigger flow-acoustic resonance in deep cavity configurations.

To date, most numerical studies have focused primarily on orthogonal geometries [45–49]. Consequently, the mechanisms governing noise generation in turbulent flows over deep and inclined cavities in resonance remain poorly understood. In this paper, we will addresses these gaps by employing wall-resolved large-eddy simulations (LES) to examine the distinct vortex dynamics and noise generation process in both orthogonal and inclined configurations. In particular, the primary objective of this study is to explore the markedly different aeroacoustic responses of inclined cavities compared to their orthogonal counterparts. For the subsequent discussions, three angles of inclination ($\alpha = 30°$, $60°$, and $90°$) and two flow speeds ($M_\infty = 0.2$ and 0.3) have been selected to highlight the unique aeroacoustic behaviours of inclined cavity flows. However, it is important to note that the mechanisms driving the transition of the aeroacoustic response across critical Mach numbers or optimal inclination angles are not the central focus of this paper.

This paper is structured and written in the following order. Section II outlines the computational setup and methods employed in this study. Sections III and IV present a detailed investigation of the acoustic and hydrodynamic fields around the cavity configurations. In Section V, the focus shifts to acoustic amplifications and source-sink cancellations through aeroacoustic resolvent analysis, with particular attention given to the critical role of the ratio of acoustic particle displacement to momentum thickness in defining distinct resonance behaviours. Finally, concluding remarks are provided in Section VI.

II. DESCRIPTION OF PROBLEM AND THE COMPUTATIONAL SET-UP

The present study investigates the cavity section with a length of $L/h = 0.608$ and depth of $D/h = 1.6$, enclosed in a channel with a height of $2h$, as shown in figure 1. The Reynolds number based on the cavity opening length, $L = 0.038$ m, is set to $Re_\infty = 261,891$ and a freestream Mach number of $M_\infty = 0.3$ based on the ambient speed of sound (for air) of $a_\infty = 340.2$ m/s and the reference temperature of $T_\infty = 288$ K are also considered in this work. The current numerical investigation employs a high-resolution implicit large-eddy simulation (ILES) method based on a wavenumber-optimized discrete filter [50]. The filter is applied directly to the solution (conservative variables) at every time step and acts as an implicit sub-grid scale (SGS) model that enforces the dissipation of scales smaller than the filter cutoff wavelength. Garmann et al. [51] performed an extensive analysis of the ILES technique compared to the traditional implementation of an explicit SGS model and concluded that ILES simulations can correctly capture the flow physics when the grid is subjected to an appropriate resolution.

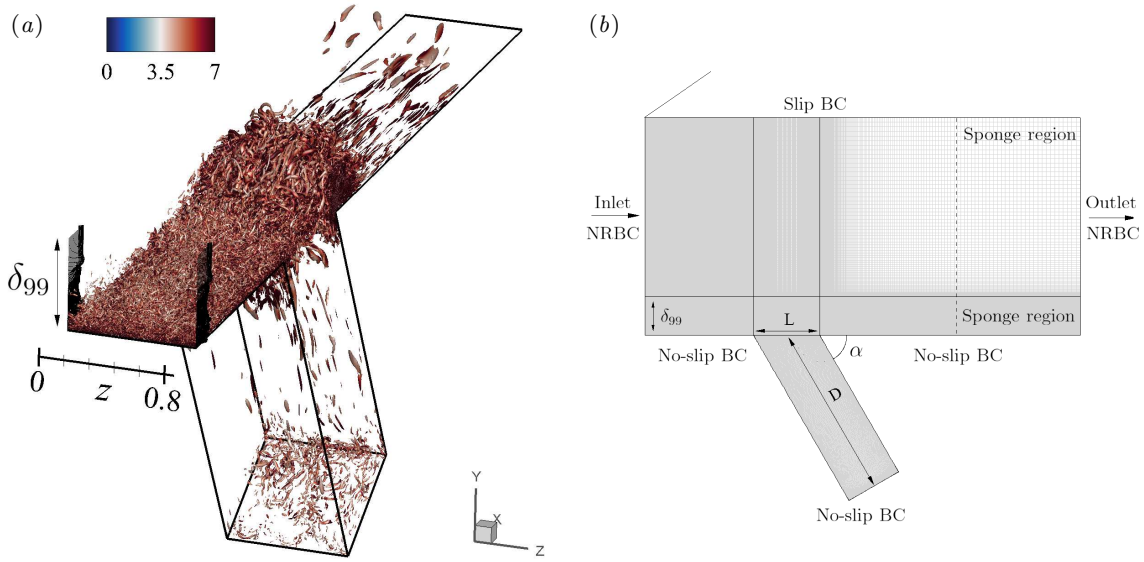

FIG. 1. Visualizations of the current computational domain of the deep and inclined cavity configuration enclosed in a channel. (a) Instantaneous non-dimensional Q-criterion iso-surfaces ($Q = 5$) coloured by non-dimensional vorticity magnitude ($|\omega_i|$), unveiling three-dimensional vortices within the turbulent boundary layer. (b) A spanwise view of the computational domain used in the current numerical investigation. The cavity length and depth are denoted by L and D, respectively.

A. Governing equations and numerical methods

In this work, the full 3-D compressible Navier-Stokes equations (with a source term for sponge layers included) are used, which can be expressed in a conservative form, transformed onto a generalised coordinate system as

$$\frac{\partial}{\partial t}\left(\frac{\boldsymbol{Q}}{J}\right)+\frac{\partial}{\partial \xi_i}\left(\frac{\boldsymbol{E}_j-Re_\infty^{-1}M_\infty \boldsymbol{F}_j}{J}\frac{\partial \xi_i}{\partial x_j}\right)=-\frac{a_\infty}{L}\frac{\boldsymbol{S}}{J}, \tag{1}$$

where the indices $i = 1, 2, 3$ and $j = 1, 2, 3$ denote the three dimensions. The vectors of the conservative variables, inviscid and viscous fluxes (that account for losses due to viscous dissipation and thermal conduction), are given by

$$\left.\begin{aligned}\boldsymbol{Q}&=[\rho,\rho u,\rho v,\rho w,\rho e_\mathrm{t}]^T,\\ \boldsymbol{E}_j&=[\rho u_j,(\rho u u_j+\delta_{1j}p),(\rho v u_j+\delta_{2j}p),(\rho w u_j+\delta_{3j}p),(\rho e_\mathrm{t}+p)u_j]^T,\\ \boldsymbol{F}_j&=[0,\tau_{1j},\tau_{2j},\tau_{3j},u_i\tau_{ji}+q_j]^T,\end{aligned}\right\} \tag{2}$$

with the stress tensor and heat flux vector written as

$$\tau_{ij}=\mu\left(\frac{\partial u_i}{\partial x_j}+\frac{\partial u_j}{\partial x_i}-\frac{2}{3}\delta_{ij}\frac{\partial u_i}{\partial x_i}\right),\quad q_j=\frac{\mu}{(\gamma-1)Pr}\frac{\partial T}{\partial x_j}, \tag{3}$$

where $\xi_i = \{\xi, \eta, \zeta\}$ are the generalised coordinates, $x_j = \{x, y, z\}$ are the Cartesian coordinates, δ_{ij} is the Kronecker delta, $u_j = \{u, v, w\}$, $e_\mathrm{t} = p/[(\gamma-1)\rho]+u_j u_j/2$ and $\gamma = 1.4$ for air. The local dynamic viscosity μ is calculated by using Sutherland's law [52]. In the current set-up, ξ, η and ζ are aligned in the streamwise, vertical and spanwise directions, respectively. The Jacobian determinant of the coordinate transformation (from Cartesian to the generalised) is given by $J^{-1} = |\partial(x, y, z)/\partial(\xi, \eta, \zeta)|$ [53]. The extra source term $\boldsymbol{S}$ on the right-hand side of (1) is non-zero within the sponge layer only, which is described in Kim *et al.* [54, 55]. In this paper, the freestream Mach and Reynolds numbers are defined as $M_\infty = u_\infty/a_\infty$ and $Re_\infty = \rho_\infty u_\infty L/\mu_\infty$ where $a_\infty = \sqrt{\gamma p_\infty/\rho_\infty}$ is the ambient speed of sound and u_∞ is the speed of the freestream mean flow. The governing equations are non-dimensionalised based on the streamwise cavity opening length $L = 38$ mm for length scales, the ambient speed of sound a_∞ for velocities, L/a_∞ for time scales and $\rho_\infty a_\infty^2$ for pressure, unless otherwise notified. Temperature, density and dynamic viscosity are normalised by their respective ambient values: T_∞, ρ_∞ and μ_∞.

The governing equations given above are solved using high-order accurate numerical methods specifically developed for aeroacoustic simulation on structured grids. The flux derivatives in space are calculated based on fourth-order

pentadiagonal compact finite difference schemes with seven-point stencils [56]. Explicit time advancing of the numerical solution is carried out using the classical fourth-order Runge-Kutta scheme with a CFL number of 0.95. Numerical stability is maintained by implementing sixth-order pentadiagonal compact filters for which the cutoff wavenumber (normalized by the grid spacing) is set to 0.85π. In addition to the sponge layers used, characteristics-based non-reflecting boundary conditions (NRBC) based on [57] are applied at the inflow and outflow boundaries to prevent any outgoing waves from returning to the computational domain. Periodic conditions are used across the spanwise boundary planes unless otherwise stated. Slip (no penetration) and no-slip wall boundary conditions based on [58] are applied at the top and bottom channel walls, respectively. The top wall boundary is intended to replicate an existing experimental set-up at the University of Southampton. Those who use a different boundary setting on the top boundary, either experimental or computational, will need to take the difference into consideration when they attempt to compare the data.

The computation is parallelized via domain decomposition and message passing interface (MPI) approaches. The compact finite difference schemes and filters used are implicit in space due to the inversion of pentadiagonal matrices involved, which requires a precise and efficient technique for parallelization to avoid numerical artifacts that may appear at the subdomain boundaries. A recent parallelization approach based on quasi-disjoint matrix systems [59] offering super-linear scalability is used in the present paper.

B. Simulation set-up and discretisation of the problem

The cavity geometry and the computational domain used in this work comprises $x/L \in [-1.64, 4.93]$ in the streamwise direction, $y \in [-2.63, 3.29]$ in the vertical direction and $z/L \in [0, 0.822]$ in the spanwise direction. The entire computational domain; the inner region (physical domain) where meaningful simulation data are obtained; and, the sponge layer zone is defined as

$$\left.\begin{aligned} \mathcal{D}_{\infty} &= \{\boldsymbol{x} \,|\, x/L \in [-1.644, 4.934], y \in [-2.632, 3.289], z/L \in [0, 0.822]\}, \\ \mathcal{D}_{\text{physical}} &= \{\boldsymbol{x} \,|\, x/L \in [-1.644, 3.289], y \in [-2.632, 3.289], z/L \in [0, 0.822]\}, \\ \mathcal{D}_{\text{sponge}} &= \mathcal{D}_{\infty} - \mathcal{D}_{\text{physical}}. \end{aligned}\right\} \tag{4}$$

The physical domain, $\mathcal{D}_{\infty}$ consists of a deep cavity with an aspect ratio of $D/L = 2.632$ enclosed in a straight rectangular channel with a channel half-height of $h/L = 1.644$. The channel region is discretised by $960 \times 290 \times 480$ grid points in streamwise, vertical, and spanwise directions. A total of $240 \times 240 \times 480$ grid points are used in the streamwise, vertical and spanwise directions, respectively, in the cavity region. The mesh in the wall-normal direction is refined close to the viscous wall $y^+ \approx 1$ to maintain a sufficiently high level of near-wall grid resolution throughout the viscous wall surfaces.

Re_{∞}	M_{∞}	α	δ^*/L	θ/L	H
174,594	0.2	90°	0.0434	0.0350	1.24
174,594	0.2	60°	0.0458	0.0368	1.25
174,594	0.2	30°	0.0442	0.0355	1.24
261,891	0.3	90°	0.0379	0.0312	1.22
261,891	0.3	60°	0.0447	0.0360	1.24
261,891	0.3	30°	0.0408	0.0332	1.23

TABLE I. The boundary layer information for the current cavity simulations measured at $x = -0.1$.

The inlet is located at $x/L = -1.664$ upstream of the cavity, where the turbulent inflow data is injected. The outflow boundary is placed at a relatively remote location downstream from the cavity, allowing a sufficient distance for the vortices to dissipate. A precursor simulation is employed to generate the prerequisite turbulent inflow data for the cavity simulation. The precursor simulation domain size ($L_x \times L_y \times L_z$) was set to $4\delta_{99} \times 1\delta_{99} \times 2\delta_{99}$ with $480 \times 240 \times 480$ grid points in the streamwise, vertical and spanwise directions, respectively. The initial boundary layer thickness, δ_{99} is determined analytically based on Na and Lu [60], and the channel flow is initialised with the turbulent mean flow profile according to Spalding [61]. In this precursor channel flow simulation, periodic boundary conditions are applied in streamwise and spanwise directions, and a streamwise pressure gradient is applied to maintain the desired mass flow rate. The precursor simulation is completed when the mean flow profile is converged, and the obtained instantaneous flow solutions are injected into the cavity simulation through the inlet plane. Figure 2 shows a close agreement of the time-averaged turbulent velocity profile and the Reynolds stresses between the current half-channel

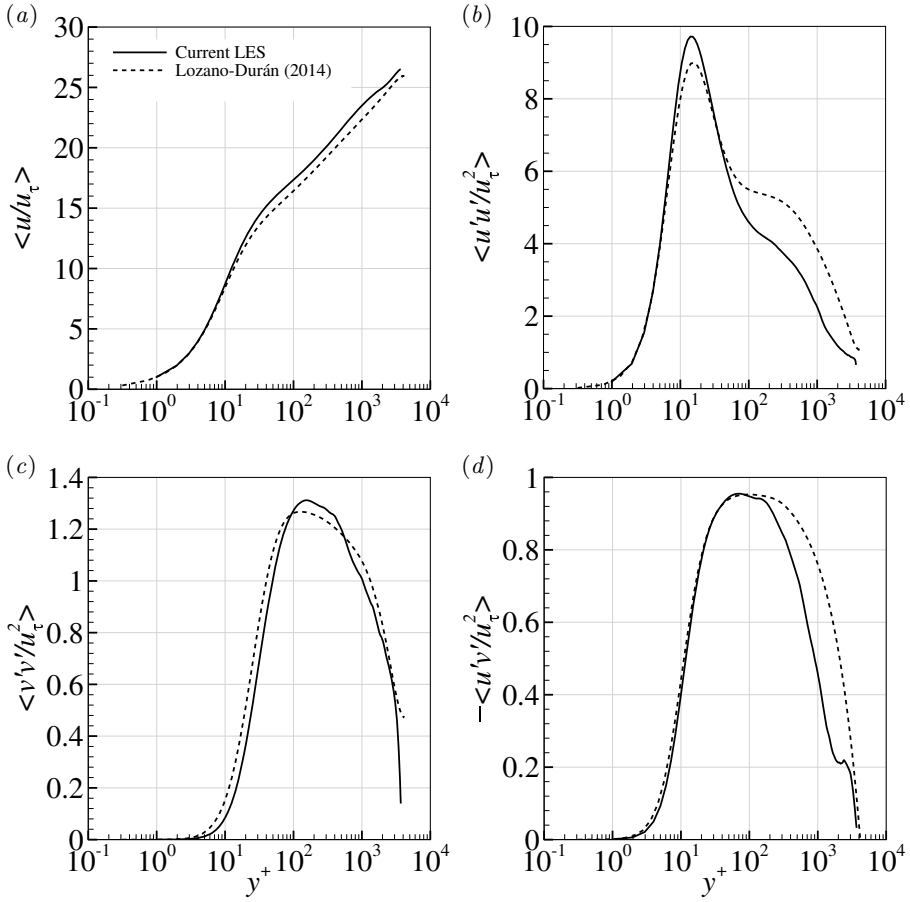

FIG. 2. (a) Time-averaged velocity profile of the turbulent boundary layer; and (b–d) Reynolds stresses obtained from the current precursor half-channel LES ($Re_\tau \approx 3900$), compared with the full-channel DNS ($Re_\tau \approx 4200$) by Lozano-Durán and Jiménez [62].

LES and a full-channel DNS by Lozano-Durán and Jiménez [62], conducted at $Re_\tau \approx 3900$ and 4200, respectively. The boundary layer data for the current simulations measured at $x = -0.1$ (10% away from the upstream cavity corner), are listed in Table I.

C. Definition of variables for statistical analysis

Data processing and analysis are performed upon the completion of the simulation. The main property required in this study is the power spectral density (PSD) function of the pressure fluctuations around the cavity. To facilitate the following discussions, we defined the pressure fluctuations here as

$$p'(\boldsymbol{x}, t) = p(\boldsymbol{x}, t) - \overline{p}(\boldsymbol{x}), \tag{5}$$

where $\overline{p}(\boldsymbol{x})$ is the time-averaged pressure field. Following the definitions used in Goldstein [63], the PSD functions of the pressure fluctuations (based on frequency and one-sided) are then calculated by

$$S_{pp}(\boldsymbol{x}, f) = \lim_{T\to\infty} \frac{\hat{p}(\boldsymbol{x}, f, T)\hat{p}^*(\boldsymbol{x}, f, T)}{T}, \tag{6}$$

where $\hat{p}$ is an approximate Fourier transform of p, respectively, based on the following definition:

$$\hat{p}(\boldsymbol{x}, f, T) = \int_{-T}^{T} p'(\boldsymbol{x}, t) e^{-2\pi i f t}\, \mathrm{d}t, \tag{7}$$

and, '$*$' denotes a complex conjugate. Similarly, the magnitude and the respective phase of the single-sided Fourier

transform pressure field are calculated by

$$|p(\boldsymbol{x}, f, T)| = 2\sqrt{\hat{p}(\boldsymbol{x}, f, T)\hat{p}^*(\boldsymbol{x}, f, T)}, \tag{8}$$

$$\Phi_p(\boldsymbol{x}, f, T) = \arctan\left\{\frac{\mathrm{Im}[\hat{p}(\boldsymbol{x}, f, T)]}{\mathrm{Re}[\hat{p}(\boldsymbol{x}, f, T)]}\right\}. \tag{9}$$

In the above equations, T represents the half-length of the time signals used for the approximate Fourier transform. The same procedures and notation are used for other field quantities later in this paper.

D. Aeroacoustic analysis tools based on APEs

The Acoustic Perturbation Equations (APEs) proposed by Ewert and Schröder [64] have been successfully demonstrated as a useful hybrid approach for accurately predicting acoustic propagation within cavity flows by using acoustic sources computed directly from fluid simulations [65, 66]. In this paper, we employ APEs as a linear operator to explore the dominant input-output characteristics of deep cavity systems based on the time-averaged mean flow states. To achieve this, we incorporate the APE-4 formulation, expressed as

$$\frac{\partial p'}{\partial t} + \bar{c}^2\nabla\cdot\left(\bar{\rho}\boldsymbol{u}' + \bar{\boldsymbol{u}}\frac{p'}{\bar{c}^2}\right) = \bar{c}^2 q_e, \tag{10}$$

$$\frac{\partial \boldsymbol{u}'}{\partial t} + \nabla\left(\bar{\boldsymbol{u}}\cdot\boldsymbol{u}'\right) + \nabla\left(\frac{p'}{\bar{\rho}}\right) = \boldsymbol{q_m}, \tag{11}$$

where the noise sources are given by

$$q_c = -\nabla\cdot\left(\rho'\boldsymbol{u}'\right)' + \frac{\bar{\rho}}{C_p}\frac{Ds'}{Dt}, \tag{12}$$

$$\boldsymbol{q_m} = -\left(\boldsymbol{\omega}\times\boldsymbol{u}\right)' + T'\nabla\bar{s} - s'\nabla\bar{T} - \left(\nabla\frac{\boldsymbol{u}'\cdot\boldsymbol{u}'}{2}\right)' + \left(\frac{\nabla\cdot\bar{\boldsymbol{\tau}}}{\rho}\right)'. \tag{13}$$

The variables marked with a prime symbol denote fluctuating quantities, whereas those with an overbar represent time-averaged values. Among the source terms, those encapsulating two primed quantities are generally smaller than their counterparts, and consequently, their contribution to the overall sources is considered negligible and thus omitted. In addition, considering the high Reynolds number and relatively low Mach number flow discussed in this paper, the contributions of viscosity and entropy to the sources can be safely omitted. Consequently, the Lamb vector, defined as $(\boldsymbol{\omega}\times\boldsymbol{u})'$, is considered the dominant source term. Applying these simplifications, Eq. (10) and Eq. (11) are rewritten in a compact form, expressed as

$$\frac{\partial \boldsymbol{q}'}{\partial t} = \boldsymbol{L}(\bar{\boldsymbol{q}})\boldsymbol{q}' + \boldsymbol{f}', \tag{14}$$

where $\boldsymbol{L}(\bar{\boldsymbol{q}})$ denotes the linear operator about the mean flow state $\bar{\boldsymbol{q}} = [\bar{p},\ \bar{u},\ \bar{v},\ \bar{w}]^T$ and $\boldsymbol{f}'$ represents the forcing input comprised of the Lamb vector. Accordingly, a modal perturbation of the form

$$\boldsymbol{q}'(x, y, z, t) = \hat{\boldsymbol{q}}(x, y)\exp i(\beta z - \omega t) + \text{complex conjugate}, \tag{15}$$

is imposed to Eq. (14) to form an input-output dynamics, expressed as

$$\hat{\boldsymbol{q}}_\omega = -[i\omega\boldsymbol{I} + \boldsymbol{L}(\bar{\boldsymbol{q}})]^{-1}\hat{\boldsymbol{f}}_\omega = \boldsymbol{R}(\bar{\boldsymbol{q}};\omega)\hat{\boldsymbol{f}}_\omega. \tag{16}$$

Here, the resolvent operator $\boldsymbol{R}(\bar{\boldsymbol{q}};\omega)$ relates the input forcing (i.e., Lamb vector), $\hat{\boldsymbol{f}}_\omega$, to the output fields as acoustic quantities (i.e., acoustic pressure fields), $\hat{\boldsymbol{q}}_\omega$, in the frequency space. The complex eigenvalue is represented by $\omega = \omega_r + i\omega_i$, with the real part of the eigenvalue, ω_r, determining the physical frequency, while its imaginary component determines the radiation loss associated with the acoustic eigenmode ($\omega_i < 0$). Furthermore, the acoustic eigenmodes of the cavity systems, which may be influenced by the mean flow field [65], can be retrieved by solving the

eigenvalue problem presented in the homogeneous form of Eq. (16). Accordingly, the discretized resolvent operator is solved using singular value decomposition to determine the directions spanned by the forcing input and the state output vectors, such as

$$\boldsymbol{R}(\bar{q};\omega) = \hat{\boldsymbol{U}}\boldsymbol{\Sigma}\hat{\boldsymbol{V}}^{H}, \tag{17}$$

where $\hat{\boldsymbol{U}} = [\hat{U}_1,\ \hat{U}_2,\ \hat{U}_3,\ \ldots]$ and $\hat{\boldsymbol{V}} = [\hat{V}_1,\ \hat{V}_2,\ \hat{V}_3,\ \ldots]$ provide the leading optimal sets of responses and the corresponding forcing mode vectors. The amplification gains of the leading optimal sets are determined by the corresponding singular values $\boldsymbol{\Sigma} = \mathrm{diag}(\sigma_1,\ \sigma_2,\ \sigma_3,\ \ldots)$, which are arranged in descending order. The superscript H in Eq. (17) indicates the Hermitian transpose operation. In this study, non-penetrating boundary conditions (i.e., zero wall-normal velocity perturbation) are enforced at the wall. Additionally, non-reflecting characteristic boundary conditions introduced by Thompson [67, 68] and damping sponge regions are used in combination to minimize artificial numerical reflections. The approximation of spatial derivatives was achieved using a standard second-order finite difference scheme. Finally, the eigenvalues and eigenvectors of the linear operator were retrieved via the Krylov-Schur algorithm [69]. All eigenmodes presented in this paper achieved convergence within a tolerance level of $||\omega\hat{\boldsymbol{Q}} - \boldsymbol{L}\hat{\boldsymbol{Q}}|| \leq O(10^{-14})$.

III. PRESSURE FLUCTUATIONS AND OSCILLATION FREQUENCIES

The self-sustained fluid-resonant oscillation in deep and inclined cavities arises from the interaction between shear-layer fluctuations over the cavity opening and an acoustic mode within the cavity. This interaction amplifies large-scale vortical structures, altering the flow field and producing intense acoustic pressure fluctuations. This process efficiently converts local flow energy into acoustic energy and is illustrated in Figure 3.

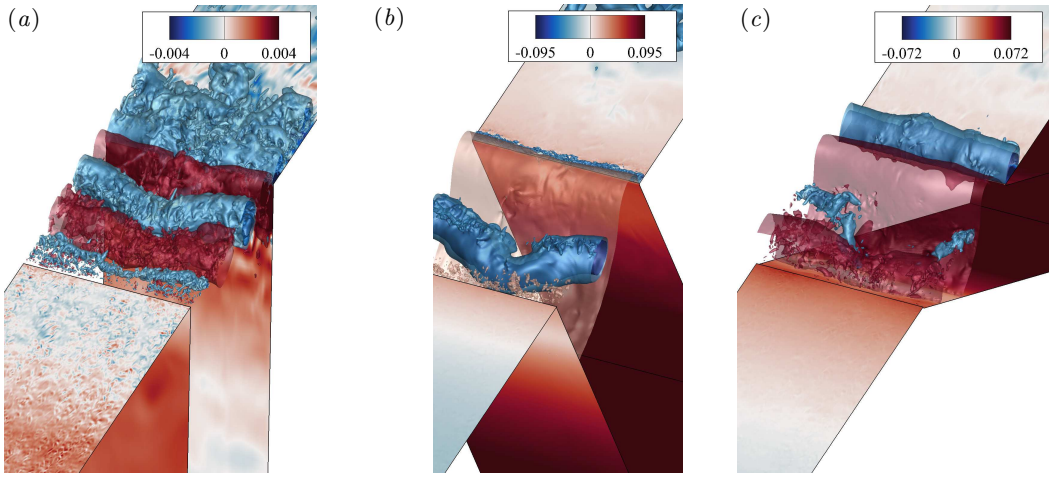

FIG. 3. Large-scale vortical structures are visualized through iso-contours of instantaneous pressure fluctuations, with the flow direction from left to right. Surface contours of wall-pressure fluctuations reveal the prominent acoustic field emanating from deep cavities for inclination angles of (a) $\alpha = 90°$, (b) $60°$ and (c) $30°$, respectively.

This section examines the aeroacoustic behaviour of wall-pressure fluctuations in deep cavities subjected to three distinct inclination angles at two specific Mach numbers, resulting in six simulations. Initially, simulations are conducted using a turbulent inflow dataset at a Mach number of $M_\infty = 0.3$ for four million time steps, corresponding to 220 non-dimensional time units. After this period, a steady-periodic state of the wall-pressure signal is achieved at the cavity base for all inclination angles, as shown in Figure 4(a). Subsequently, the Fourier transform is applied to the pressure time signals over an additional non-dimensional time span of approximately 740 samples (collected every 0.164 time unit) from the computational data, covering a total non-dimensional time of 120. This interval captures approximately ten cycles of the lowest fundamental frequency. The resulting time signals are nearly periodic, and any steady component is eliminated prior to the Fourier transform. Various windowing functions have been tested, and the results exhibit comparable spectrum compositions. The procedures are then repeated with a turbulent inflow dataset at a Mach number of $M_\infty = 0.2$, as previously studied by Ho and Kim [23]. The corresponding wall-pressure signals for each inclination angle are shown in Figure 4(b). Notably, the time signals from inclined cavities exhibit highly periodic oscillations, highlighting the self-sustaining nature of the oscillation at both Mach numbers.

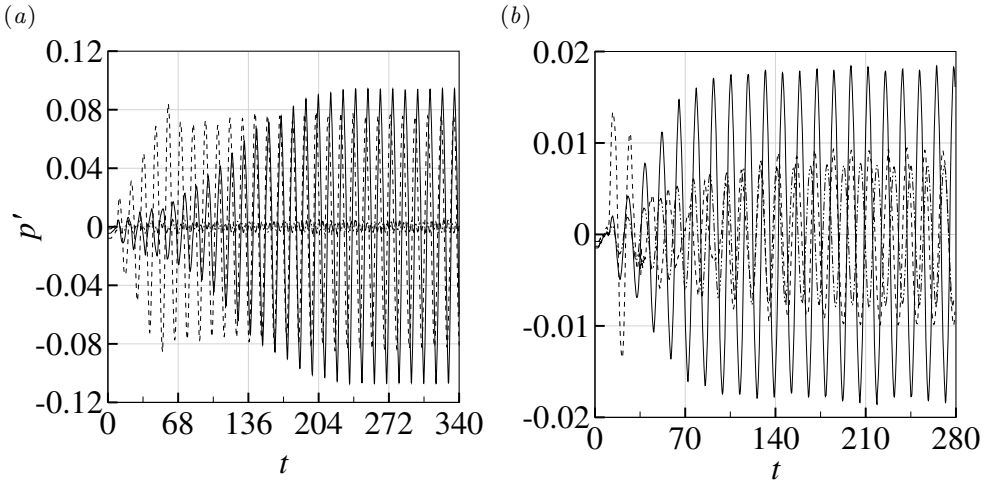

FIG. 4. The spanwise-averaged time signals of pressure fluctuations on the base surface of deep cavities are presented for (-···-) $\alpha = 90°$, (——) 60° and (- - -) 30° at free-stream Mach numbers of (a) $M_\infty = 0.3$ and (b) 0.2, respectively.

The power spectra of wall-pressure fluctuations at $M_\infty = 0.2$ are depicted in figure 5(b). The figure shows that all three cavity cases ($\alpha = 30°$, 60°, and 90°) exhibit flow-acoustic resonance closely associated with the fundamental frequency ($St = 0.386$). The authors have previously investigated the orthogonal cavity flow characteristics at this fundamental frequency [23], where the critical Mach number for this particular cavity geometry ($D/L = 2.632$) and inflow condition ($\theta/L = 0.0345$) was estimated to be $M_\infty = 0.2$. This critical condition was understood to result from a lock-in event between the 1st Rossiter's streamwise feedback and depthwise acoustic resonance modes. Therefore, any deviation in flow speed from this Mach number is expected to produce a sub-optimal flow-acoustic resonance. This assumption is supported by the weaker acoustic response generated from the same orthogonal cavity at $M_\infty = 0.3$, as shown in figure 5(a). This weak resonance at $St = 0.849$ coincides with the 2nd Rossiter's mode, i.e. $St_n = (n-1/4)/(M_\infty+1/\kappa)$ where $\kappa = 0.57$ and $n = 2$. However, contrary to previously established expectations, the inclined cavities at this Mach number produce an entirely unexpected result. First, the fundamental peak frequency shifted to a lower value of $St = 0.276$ which the Rossiter's model did not predict. It is noteworthy that previous experimental studies on orthogonal deep cavities by [8, 9, 24, 25] also reported a critical resonance occurring at the similar frequency, which does not conform to existing flow-acoustic resonance theories. Second, and more importantly, the inclined cavities generated a significant increase in the peak amplitude by nearly 30 dB compared to the orthogonal cavity case and by more than 10 dB even compared to the "optimal" flow-acoustic resonance at $M_\infty = 0.2$. The observed shift in the fundamental peak frequency and substantial increase in peak amplitude for inclined cavities at $M_\infty = 0.3$ suggest novel flow-acoustic interaction mechanisms at play. Consequently, this paper aims to investigate the underlying physical processes responsible for these unexpected and profound results.

Figure 6 presents snapshots of the spanwise-averaged instantaneous pressure fluctuations captured at four sequential time intervals, each separated by $T/4$, where $T = 1/f_p$ represents the oscillation period corresponding to the tonal frequency identified in the pressure spectra of Figure 5(a). These snapshots illustrate the synchronization between shear-layer fluctuations and instantaneous pressure oscillations within the deep and inclined cavities. Here, we define a surface-averaged acoustic pressure at the cavity base to determine the phase of the resonance cycle:

$$\chi(t) = \frac{1}{A_b}\int_{A_b} p'(\boldsymbol{x}_b, t)\mathrm{d}A, \tag{18}$$

where x_b and A_b denote the Cartesian coordinates on the surface area of the cavity base, respectively. For brevity, the following discussion primarily focuses on the $\alpha = 60°$ inclined cavity. Figure 6(a) shows the beginning of an oscillation cycle of χ, during which a distinct large-scale vortex is positioned slightly above the cavity opening, as revealed by the low-pressure zone near the downstream corner. At this point, nearly complete destructive interference occurs between the reflected compressive wave (i.e., $p' > 0$) and the incident rarefaction acoustic wave (i.e., $p' < 0$), resulting in an acoustic pressure equilibrium within the cavity (i.e., $\chi = 0$). Shortly after this, the rarefaction acoustic wave from the cavity base begins to dominate the cavity and the shear layer moves downward. Also, as the large-scale vortical structure impinges on the downstream corner, additional rarefaction waves are generated. These rarefaction waves keep reducing the acoustic pressure within the cavity until it reaches its minimum value, as depicted in figure 6(b). Meanwhile, a low-pressure region appears near the upstream corner, indicating the emergence of the next

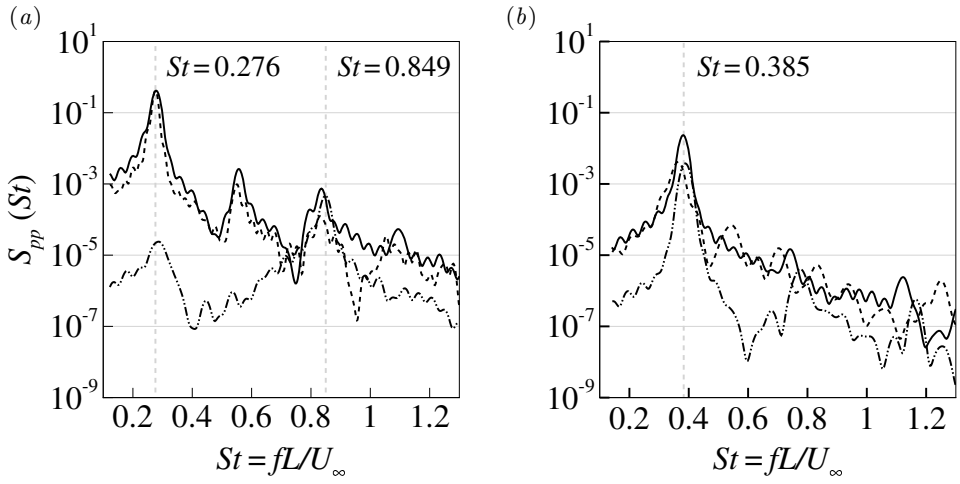

FIG. 5. The power spectral density (PSD) of the spanwise-averaged time signals of wall-pressure fluctuations on the base surface of deep cavities is presented for (-···-) $\alpha = 90^{\circ}$, (——) 60° and (- - -) 30° at free-stream Mach numbers (a) $M_{\infty} = 0.3$ and (b) 0.2, respectively.

vortical structure. Also, the main streamlines start to collide with the downstream corner, meaning that the flow momentum decreases and the pressure increases there, as shown in figure 6(c). At this instant ($\chi = 0$), another complete destructive interference occurs between the compressive and rarefaction waves. Afterwards, the compressive waves begins to dominate the cavity until χ reaches its maximum value as depicted in figure 6(d). During this process, the main streamlines gradually rise from the downstream corner, the flow stagnation lessens and the large-scale vortex convects downstream before being ejected from the cavity - going back to figure 6(a).

The discussions above implicitly identified two main types of pressure fluctuations, namely the local hydrodynamic fluctuations near the cavity opening and acoustic fluctuations surrounding the cavity. The distinction between these two components can be further clarified through the magnitude and phase distributions of the Fourier-transformed pressure fluctuations. Accordingly, figure 7 shows that the pressure field inside the cavity appears to be primarily stationary (i.e., constant phase), with a maximum magnitude (i.e., a pressure node) consistently located at the cavity base across all inclinations. This evidence suggests that the pressure field inside the cavity is predominantly acoustic in nature and contributed by the depthwise acoustic resonances. Furthermore, these resonances are highly localized within the inclined cavities and resemble the "nearly trapped acoustic mode", that exhibits minimal radiation losses, according to Koch [16].

To facilitate subsequent investigations, we decompose the pressure fluctuations around the cavity into their hydrodynamic and acoustic components using momentum potential theory (MPT) developed by Doak [70]. Essentially, Doak's MPT separates the momentum density, $\rho\boldsymbol{u}$, into rotational and irrotational components through a Helmholtz decomposition. The Helmholtz decomposition of $\rho\boldsymbol{u}$ may be written as

$$\rho\boldsymbol{u} = \boldsymbol{B} - \nabla\psi, \quad \nabla \cdot \boldsymbol{B} = 0, \tag{19}$$

where $\boldsymbol{B}$ and $\nabla\psi$ are the solenoidal and irrotational components of $\rho\boldsymbol{u}$, respectively. Substituting Eq. (19) into the continuity equation yields a Poisson equation for the irrotational component, with a source term dependent on density fluctuation,

$$\nabla^2\psi = \frac{\partial\rho}{\partial t}. \tag{20}$$

For a single phase continuum fluid, ψ is separated into acoustic component (irrotational and isentropic, denoted ψ_A) and entropic component (irrotational and isobaric, ψ_E) components, governed by the exact equations

$$\psi = \psi_A + \psi_E, \quad \nabla^2\psi_A = \frac{1}{c^2}\frac{\partial\rho}{\partial t}, \quad \nabla^2\psi_E = \frac{\partial\rho}{\partial E}\frac{\partial E}{\partial t}. \tag{21}$$

Considering the low Mach number in this study, the entropy (thermal) contribution is assumed to be relatively small compared to the acoustic contribution, and therefore ψ_E is not included in the subsequent calculation. Then, the momentum equation in terms of the hydrodynamic and acoustic components is obtained by substituting Eq. (19)

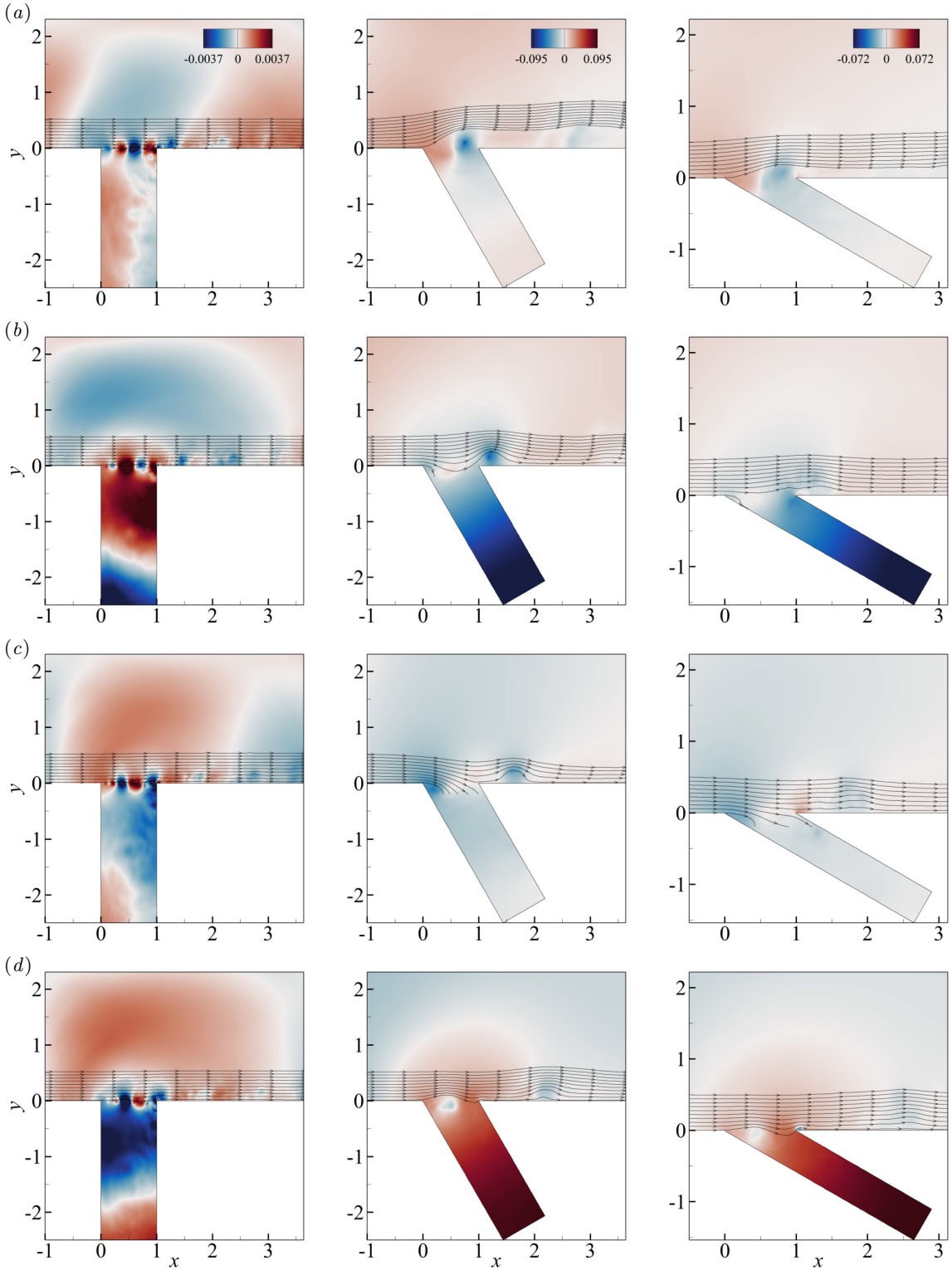

FIG. 6. Snapshots of the spanwise-averaged instantaneous pressure fluctuations p' are shown with superimposed streamlines. The snapshots are taken at time intervals of $T/4$ between successive plots (a) to (d), where T represents the oscillation cycle period of χ. The first, second, and third columns correspond to deep cavities with $\alpha = 90°$, $60°$ and $30°$, respectively. Here, compressive ($p' > 0$) and rarefaction ($p' < 0$) acoustic waves are visualized as red and blue regions within the interior of the cavity.

into the momentum equation, expressed as

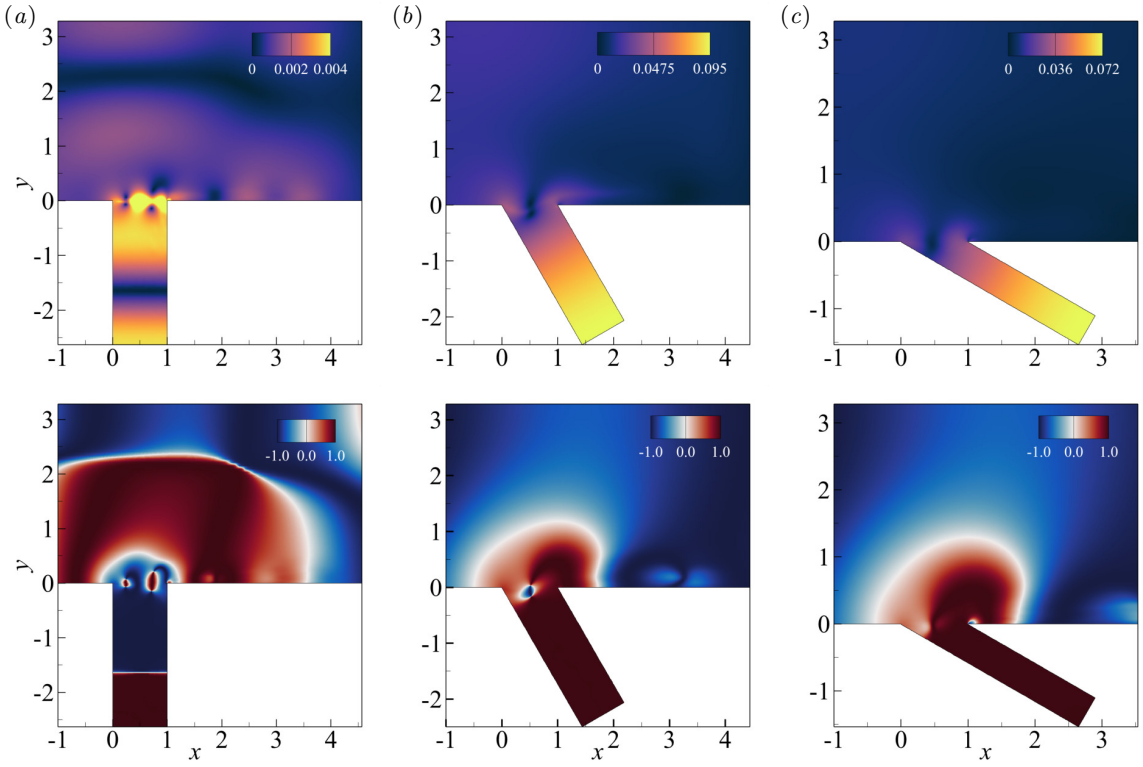

FIG. 7. The spatial distribution of Fourier-transformed pressure fluctuations at the tonal frequency is shown for deep cavities with (*a*) $\alpha = 90°$, (*b*) 60° and (*c*) 30°. The top row of the contour plots represents the magnitude $|p'|$, while the bottom row of the contour plots represents the cosine of the phase $\cos[\Phi_{p'}(\boldsymbol{x}, f) - \Phi_{\chi}(\boldsymbol{x}, f)]$. Here, $\Phi_{\chi}(\boldsymbol{x}, f)$ denotes the phase of the Fourier transform of χ, as defined in Eq. (18).

$$\frac{\partial}{\partial t}(\boldsymbol{B} - \nabla\psi) + \nabla \cdot \left[\frac{(\boldsymbol{B} - \nabla\psi)(\boldsymbol{B} - \nabla\psi)}{\rho} - \tau_{ij}\right] + \nabla p = 0. \tag{22}$$

By taking the divergence of Eq. (22), the Poisson equation for the hydrodynamic pressure fluctuation, p'_H

$$\nabla^2 p'_H = S_H + \tilde{S}_H, \tag{23}$$

and the Poisson equation for the acoustic pressure fluctuation, p'_A

$$\nabla^2 p'_A = S_A + \tilde{S}_A, \tag{24}$$

are derived. Accordingly, the hydrodynamic and acoustic pressure fluctuations are obtained by solving the Poisson equations in Eq. (23) and Eq. (24), respectively. The numerical implementation is described extensively in [23, 71] and the evaluations of the linear (S_H and S_A) and the non-linear source terms ($\tilde{S}_H$ and $\tilde{S}_A$) are detailed in [72], which are not repeated here for brevity.

Figure 8 reveals notable differences in the spatial distribution of pressure gradients for the acoustic components across orthogonal and inclined cavities. In particular, the acoustic pressure gradient tends to concentrate more intensely near the downstream corner in inclined cavities, in contrast to the symmetric distribution observed in the orthogonal cavity. This discrepancy in the spatial distribution of the acoustic pressure gradient is important for elucidating the noise generation process, which will be further discussed in Section V. Additionally, the difference in magnitude of the acoustic pressure gradient indicates that the resonant acoustic fields in inclined cavities may produce higher acoustic particle velocities compared to those in the orthogonal cavity. To quantify these observations, the induced acoustic particle velocity along the cavity opening region is approximated as being proportional to the acoustic pressure gradient, using the isentropic Euler equations [73], as expressed by

$$\frac{dv_a}{dt} = -\frac{1}{\rho}\frac{\partial p_a}{\partial y}, \tag{25}$$

where $\tilde{v}_a$ represents the estimated acoustic particle velocity and p_a is the decomposed acoustic pressure field. Then,

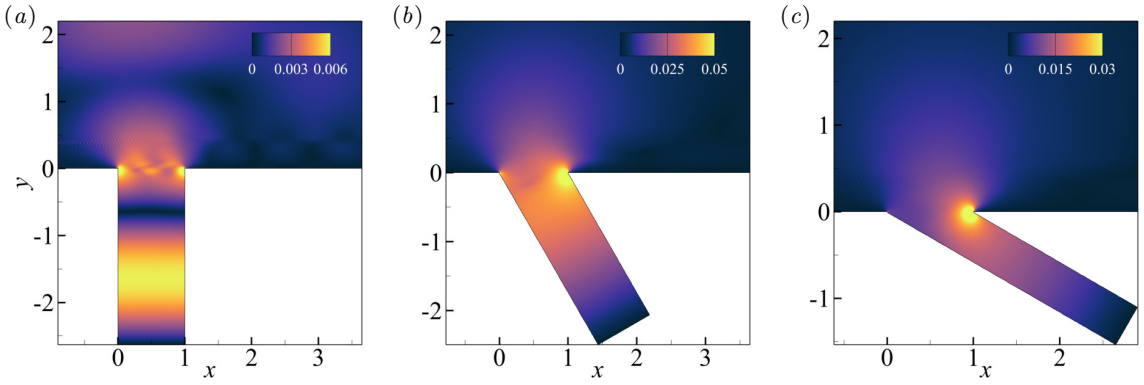

FIG. 8. The contour plots illustrate the spatial distribution of the magnitude of the decomposed Fourier-transformed pressure gradient associated with the acoustic component $|\partial p_A/\partial y|$ at the tonal frequency for (a) $\alpha = 90°$, (b) $60°$ and (c) $30°$.

by considering a modal fluctuation of the acoustic pressure and spatially averaging the acoustic particle velocity across the cavity opening, we obtain an averaged acoustic particle velocity that oscillates across the cavity opening, as given by

$$\overline{v}_a = \frac{1}{L}\int_{x=0}^{x=L} \frac{1}{2\pi f}\frac{\partial p_a}{\partial y}\,\mathrm{d}x. \tag{26}$$

At tonal frequencies, cavities with inclinations of ($\alpha = 90°$, $60°$, and $30°$) exhibit an average acoustic particle velocity across the cavity opening of approximately ($|\overline{v}_a|/u_\infty \approx 9.3\times10^{-3}$, 2.5×10^{-1}, and 1.1×10^{-1}), respectively. For inclined cavities, these amplitude levels are traditionally categorized as "high pulsation levels", according to Bruggeman [3, 74]. Previous studies by Peters [8] have demonstrated that under such extreme conditions, the resonant field can significantly alter the vortex trajectory, causing the vortex to enter and exit the cavity rather than following the parallel path of an unperturbed shear layer. These intense flow dynamics align with the temporal evolution of instantaneous pressure fluctuations and shear-layer oscillations observed in figure 6. In contrast, the acoustic particle velocity magnitude in the orthogonal cavity corresponds to "low pulsation levels", reflecting the subdued shear-layer oscillation. This behavior will be further discussed and visualized later in figure 13.

Figure 9(a) presents a comparison of pressure spectra for all cavity oscillations at $M_\infty = 0.3$, similar to that shown in figure 5(a), with frequencies here expressed in Helmholtz numbers, $He = fL/a_\infty$, to enable direct comparison with the first three least-damped acoustic modes (eigenmodes) obtained from the modal analysis of APEs. These acoustic eigenmodes are characterized by complex resonance frequencies, with the real part indicating the physical resonance frequencies and the imaginary part measuring the radiation losses (i.e., damping) of the resonances, as outlined in Subsection II D. Here, the damping levels may provide useful indications of the relative amplitudes of resonance between different modes when an identical acoustic input is imposed. It worth mentioning here that the eigenmode analysis is purely based on acoustic perturbation with no flow fluctuation (feedback) involved. The eigenmodes analysis indicates possible frequencies (or around them) at which an acoustic resonance may occur. The damping levels may be indicative of the relative amplitudes of resonance between different modes when an identical acoustic input is imposed without feedback from the flow.

Figure 9(b) shows that the tonal frequencies of the cavity oscillations at $M_\infty = 0.3$ all reside close to their respective acoustic eigenmodes, highlighting the important role of acoustic resonances in supporting the oscillation frequency in deep and inclined cavities. When comparing the orthogonal and inclined cavity cases, a 1st depthwise acoustic mode is excited in the inclined cavities which have lower radiation losses than the 2nd mode excited in the orthogonal cavity. As discussed by Koch [16], acoustic modes with higher radiation losses (i.e., a more negative imaginary part of the complex frequency) radiate and dissipate more energy into the surroundings and less energy contained within the cavity. This is indeed revealed in figure 10. The inclined cavities (1st mode) show much less leakage of acoustic energy into the far field than the orthogonal cavity (2nd mode). A higher level of acoustic (pulsation) energy contained within the inclined cavities means that they have the potential to excite the shear layer at a greater magnitude. However, the selection of oscillation frequency in deep and inclined cavities is governed by multiple factors, with the disparity in radiation losses of depthwise acoustic modes being only one contributing aspect. In the following sections, we examine how the vortex dynamics (as a result of the shear-layer perturbation) and the acoustic response of the cavity influence frequency selection, particularly at $St = 0.276$ in inclined cavities.

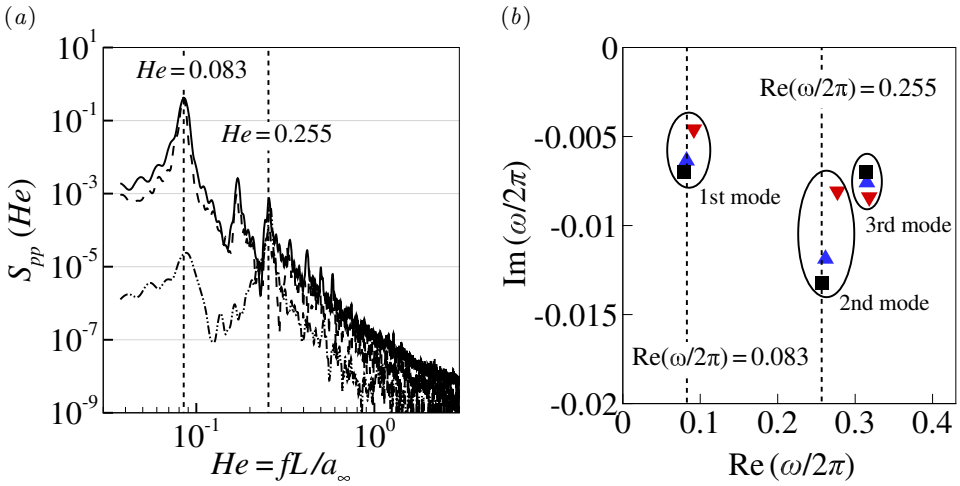

FIG. 9. Plot (a) presents the power spectral density (PSD) of the spanwise-averaged wall-pressure fluctuations for (-···-) $\alpha = 90°$, (——) 60° and (- - -) 30° at $M_\infty = 0.3$, with frequency expressed as the Helmholtz number ($He = fL/a_\infty$). The tonal frequencies from the LES, indicated by the vertical dashed lines (- - -) at $He = 0.083$ and $He = 0.255$, are compared in panel (b) with the first three least-damped depthwise acoustic modes (eigenmodes) obtained from the modal analysis of APEs for cavities with (■) $\alpha = 90°$, (▲) 60° and (▼) 30°. Note that the orthogonal cavity produced a resonance with a 2nd depthwise acoustic mode and the inclined cavities with a 1st mode. The 1st mode exhibits less radiation losses meaning that more acoustic energy is contained within the cavity (to excite the shear layer). Furthermore, the frequencies of the depthwise acoustic modes closely match the first classical acoustic quarter-wave (e.g., $He = 0.095$) and the third acoustic quarter-wave (e.g., $He = 0.285$) of a closed tube. In experimental studies, any slight discrepancies in frequency from this classical prediction are typically minimized by applying end corrections, see Yang et al [9], for example.

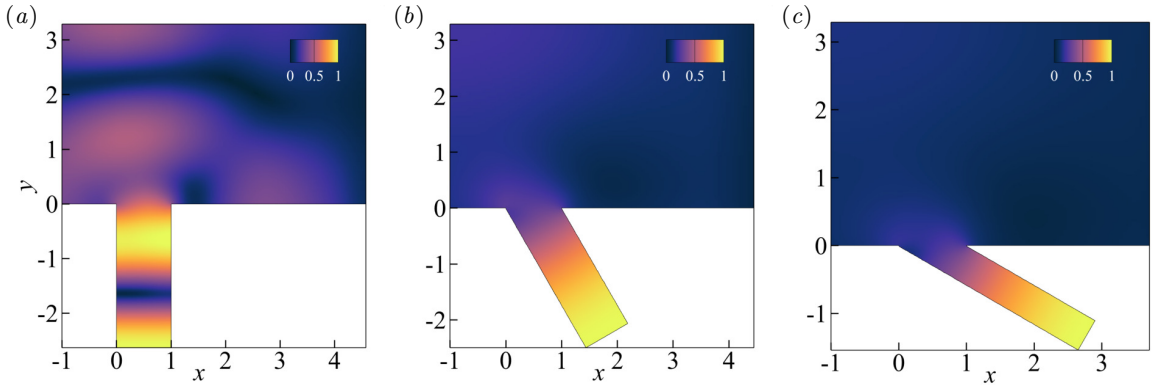

FIG. 10. The contour plots depict the spatial distribution of the pressure magnitude for the eigenmode at frequency nearest to the tonal frequency in cavities with (a) $\alpha = 90°$, (b) 60° and (c) 30°. For fair comparisons, the magnitude of the eigenvector is normalised such that it is unity at the base of the cavity.

IV. HYDRODYNAMIC FIELDS

In this section, we discuss the hydrodynamic fields near the cavity opening in detail. As mentioned, the location of the coherent vortical structure is crucial to the acoustic emission process. Therefore, an accurate description of the position and path traveled by the vortical structure, which is a function of time, is essential for this investigation. Generally, the location of the vortical structure can be approximated using the pressure minima technique, as shown in Section III. However, it is challenging to justify an accurate quantification of the hydrodynamic mode based on the number of discrete low-pressure spots [23]. To overcome this limitation, the location of the vortical structure is identified using the equivalent Q-criterion [75], which is given by

$$Q = \epsilon_{ij}\epsilon_{ji} - \frac{1}{2}\omega_i^2 \approx -\nabla^2 \tilde{p_H}/\rho_\infty, \tag{27}$$

where $\epsilon_{ij} = \frac{1}{2}(\partial u_i/\partial x_j + \partial u_j/\partial x_i)$ represents the rate of strain, ω_i denotes the vorticity of the velocity field, and $\nabla^2 \tilde{p_H}$ is the Laplacian of the hydrodynamic pressure field. This formulation offers two distinct advantages: first, Eq. (27) establishes a direct link between the velocity gradient field and the hydrodynamic pressure field to accurately pinpoint the location of the vortex. Second, the positive and negative values of the Q-criterion provide valuable insights into the strain rate and vorticity of the velocity fields, which are essential for understanding subsequent noise generation mechanisms [76].

Figure 11 shows an oscillation cycle of χ similar to that of figure 6, with particular attention now given to the vortex dynamics near the cavity opening region. The Q-criterion, calculated from Eq. (27), is plotted and superimposed with streamlines to indicate the shear-layer oscillations near the cavity opening. For brevity, we examine the vortex dynamics within the $\alpha = 60°$ inclined cavity. Figure 11(a) shows the instant when a large-scale vortex, characterized by $Q < 0$, is located slightly above the cavity opening line at the downstream corner. The vorticity-dominated region near the downstream walls is associated with low hydrodynamic pressure ($p'_H < 0$) and is visualized in figure 12. These hydrodynamic wall-pressure fluctuations act as a dipole noise source from the surface integral of Curle's equation [77], which were previously identified as the dominant noise source in both shallow and deep cavities [78, 79]. Therefore, the presence of low hydrodynamic wall-pressure fluctuations ($p'_H < 0$) correspond to generating rarefaction acoustic waves ($p'_A < 0$), which at this point destructively interfere with compressive acoustic waves ($p'_A > 0$) reflected from the cavity base during the preceding cycle. This destructive interference leads to the acoustic pressure equilibrium within the cavity (i.e., $\chi = 0$), as previously discussed in figure 6(a).

Continuing to examine the $\alpha = 60°$ case, as the large-scale vortex sweeps past the downstream corner, it induces stronger interaction with the vorticity field and the downstream walls. At this stage, the additional rarefaction waves undergo constructive interference with the acoustic waves reflected from the base of the cavity, until the large-scale vortex is completely ejected from the cavity, as shown in figure 11(b). The ejection of the vortex triggers an immediate downward flapping of the shear-layer near the upstream corner, accompanied by the emergence of small-scale vortices within the separated shear-layer. These small vortices gradually grow and merge, eventually forming a single large-scale vortex near the upstream corner, as illustrated in figure 11(c). The further downstream convection and development of this large-scale vortex before completing the feedback oscillation cycle is shown in figure 11(d). In contrast to the orthogonal cavity case, the recurring interaction between the escaping vortical structure and the downstream corner in inclined cavities mirrors the well-documented phenomenon of "vortex above corner" interaction, as reported by Tang and Rockwell [80].

Additionally, we employ the Direct Lyapunov Exponents (DLE) method introduced by Haller [81, 82] to identify the Lagrangian Coherent Structures (LCS) present in the turbulent cavity flow fields. The DLE field is defined as

$$\mathrm{DLE}_{\Delta T}(x_0, t_0) = \frac{1}{2\Delta T} \log(\sigma_T(x_0, t_0)), \tag{28}$$

where σ_T represents the square of the largest singular value of the Cauchy-Green deformation tensor such that

$$\sigma_T(x_0, t_0) = \lambda_{\max} \left(\left[\frac{\partial x(t_0 + \Delta T, x_0, t_0)}{\partial x_0} \right]^T \left[\frac{\partial x(t_0 + \Delta T, x_0, t_0)}{\partial x_0} \right] \right), \tag{29}$$

and $x(t, x_0, t_0)$ denotes the position of a particle at time t, initiating at position x_0 at time t_0. The DLE field is calculated by integrating trajectories in backward time ($\Delta T < 0$) and the ridges in the DLE field capture attracting Lagrangian coherent structures (attracting LCS) in the flow field [81]. The integration time, ΔT, is adjusted to achieve the desired level of detail in the calculation without compromising the location of the attracting LCS boundary. The DLE field is visualised in figure 13.

Based on figures 11 – 13 (also video clips provided as a supplementary material to this paper), we highlight that there is a distinctive flow mechanism in the inclined cavities which is significantly different from that of the orthogonal cavity. Firstly, the inclined cavities produce a large single vortical structure travelling across the cavity opening which manifests a 1st hydrodynamic mode. On the other hand, the orthogonal cavity exhibits two smaller vortices travelling along simultaneously, i.e. a 2nd hydrodynamic mode. In the inclined cavities, there is a pronounced level of Kelvin-Helmholtz instability and a flapping motion of the shear layer. When the shear layer is flapped downward an intense roll-up vortex is created at the upsream corner. The roll-up vortex then keeps growing in size by merging smaller eddies nearby as the shear layer flaps upward. The vortex spends a substantial amount of time in growing rather than rapidly travelling downstream (to be shown later). This results in a significantly longer cycle period. Also, due to the large size, only one vortex occupies the cavity rather than two. We suggest that these are the main reasons why the inclined cavities exhibit the 1st hydrodynamic mode which selects a lower-frequency resonance with the 1st acoustic mode. In addition, the relatively higher acoustic pulsation energy contained within the inclined cavities (as deduced from the eigenmode analysis in the previous section) may have reinforced the excitation of K-H instability and shear-layer flapping.

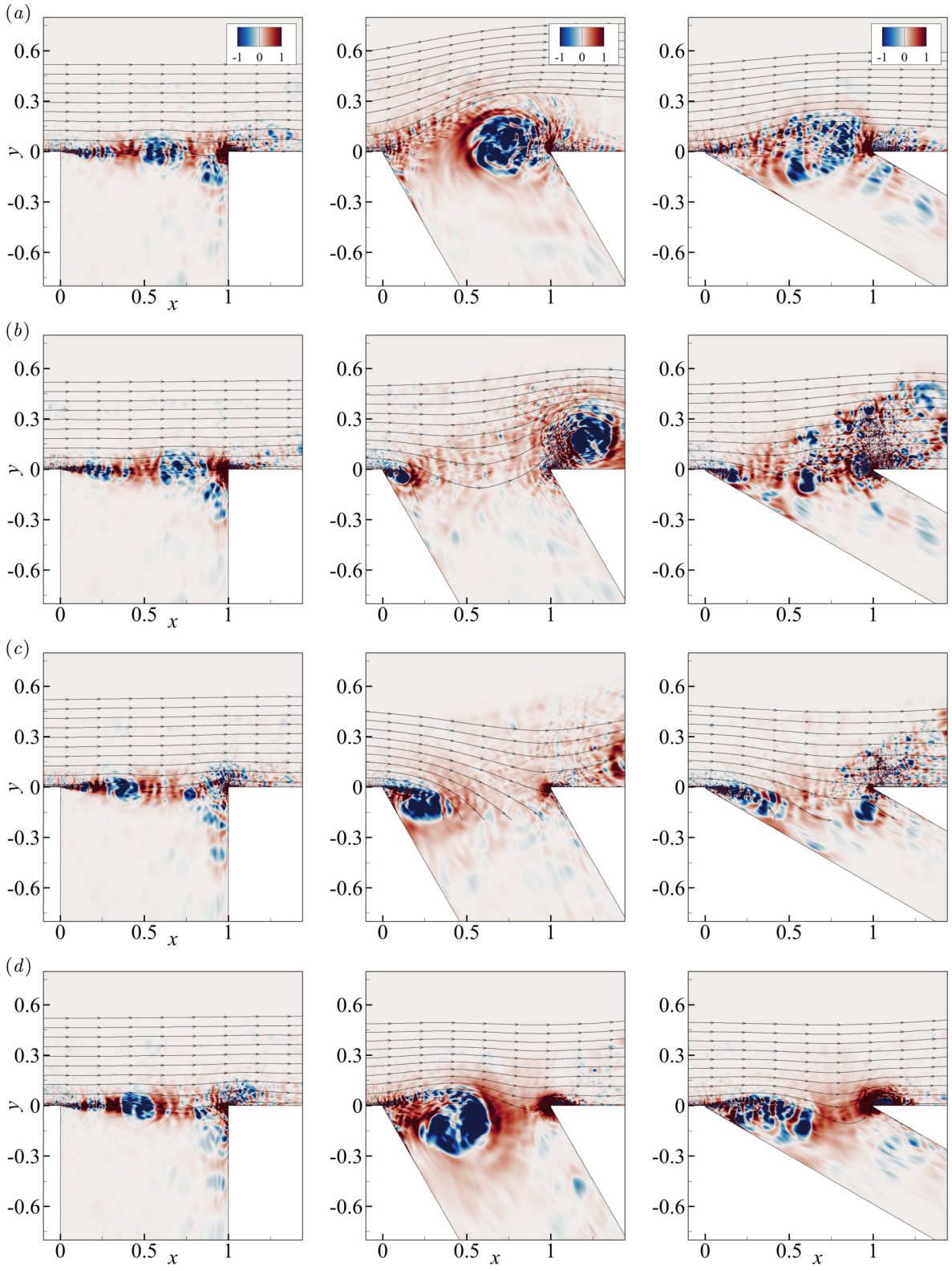

FIG. 11. Snapshots of the spanwise-averaged instantaneous Q-criterion with superimposed streamlines to signify the shear-layer undulation across the cavity opening with a time interval of $T/4$ between two successive plots from (a) to (d), where T is the period of the oscillation cycle of χ. The first, second and third columns correspond to $\alpha = 90^\circ$, 60° and 30°, respectively. For the corresponding hydrodynamic pressure fields, refer to figure 12.

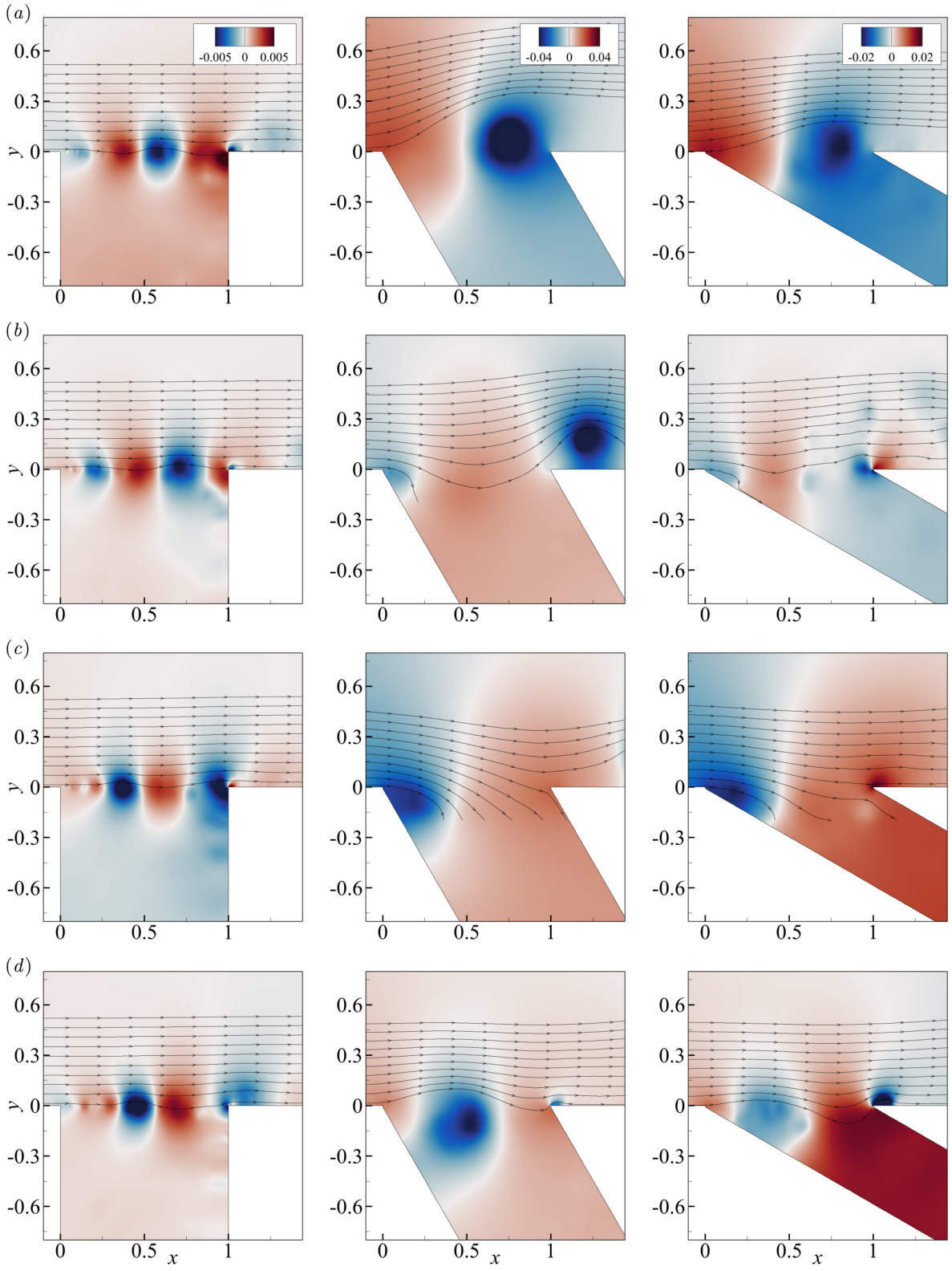

FIG. 12. Snapshots of the spanwise-averaged instantaneous hydrodynamic pressure fluctuation p'_H with superimposed streamlines to signify the shear-layer undulation across the cavity opening with a time interval of $T/4$ between two successive plots from (a) to (d), where T is the period of the oscillation cycle of χ. The first, second and third columns correspond to $\alpha = 90°$, $60°$ and $30°$, respectively.

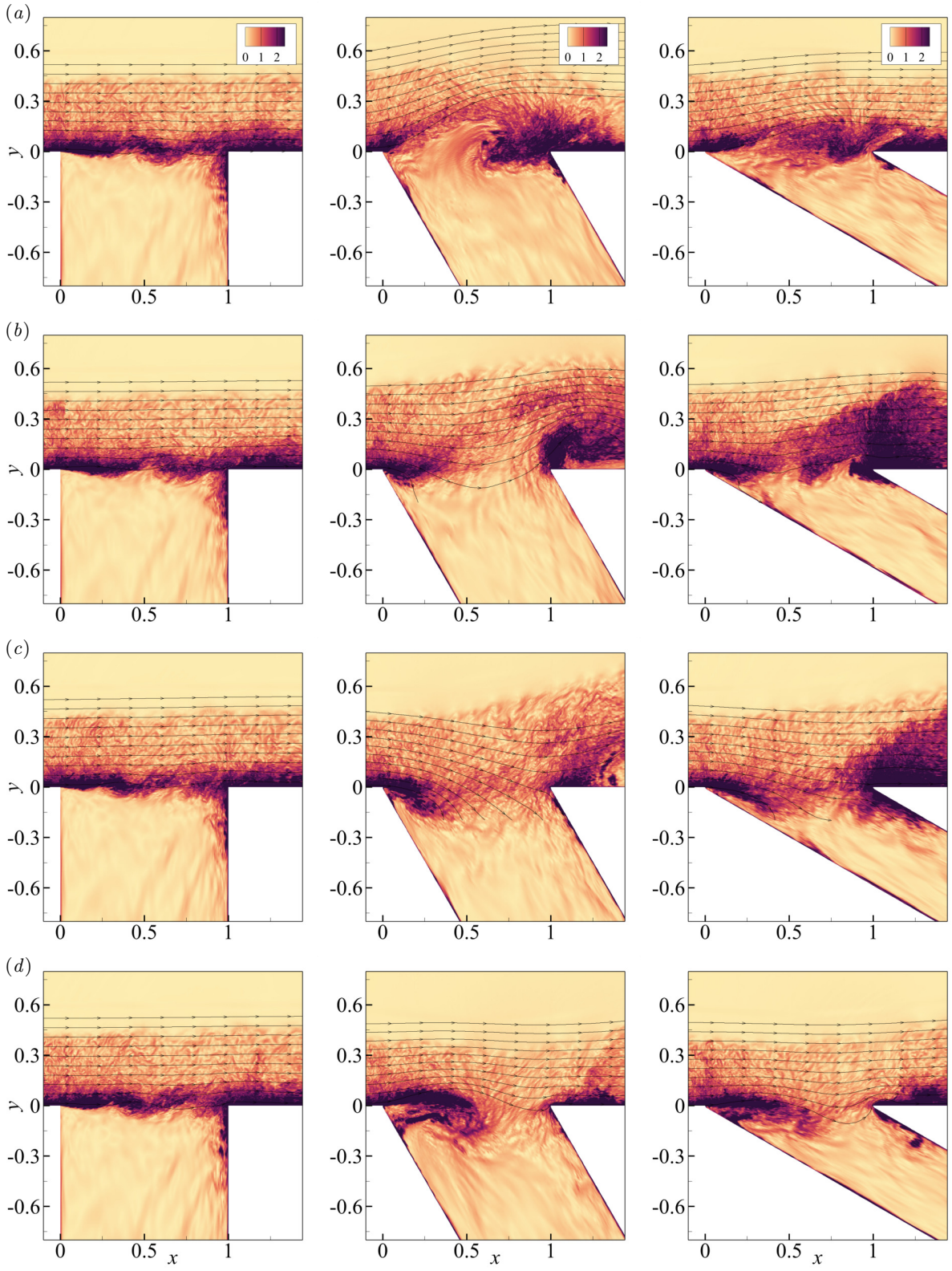

FIG. 13. Snapshots of the spanwise-averaged instantaneous DLE with superimposed streamlines to signify the shear-layer undulation across the cavity opening with a time interval of $T/4$ between two successive plots from (a) to (d), where T is the period of the oscillation cycle of χ. The first, second and third columns correspond to $\alpha = 90^\circ$, 60° and 30°, respectively. For the corresponding Q-criterion fields, refer to figure 11.

We suggest that the shear-layer flapping may be quantified by the time rate of change of mass flow rate through the cavity opening. First, based on equation 19 used in MPT, the total mass flow rate is decomposed into hydrodynamic ($\dot{m}_H$) and acoustic ($\dot{m}_A$) components, and their time rate of change are expressed as

$$\frac{d\dot{m}_H}{dt}(t) = \frac{1}{dt}\int_0^1 (\rho v)_H|_{y=0}dx = \frac{1}{dt}\int_0^1 B_y|_{y=0}dx, \tag{30a}$$

$$\frac{d\dot{m}_A}{dt}(t) = \frac{1}{dt}\int_0^1 (\rho v)_A|_{y=0}dx = -\frac{1}{dt}\int_0^1 \left.\frac{\partial \psi_A}{\partial y}\right|_{y=0} dx. \tag{30b}$$

In addition, the shear-layer flapping may also be characterised by the displacement of a streamline (emerging from the upstream corner), Δy_{sh}, measured at the center of the cavity opening, $(x, y) = (0.5, 0)$. Figure 14 shows the time history of $d\dot{m}_H/dt$, $d\dot{m}_A/dt$ and Δy_{sh} for each cavity. It is apparent that energetic shear-layer flapping is present in the inclined cavities and is almost perfectly synchronized with $d\dot{m}_A/dt$ that is induced by the depthwise acoustic resonance. Meanwhile, no contribution from the hydrodynamic component ($\dot{m}_H$) appears here, which makes sense because the net mass flow rate of solenoidal (incompressible) flow in a confined geometry should remain zero. However, the hydrodynamic component of the vertical momentum $(\rho v)_H$ offers crucial information about the vortex dynamics taking place across the cavity opening (to follow).

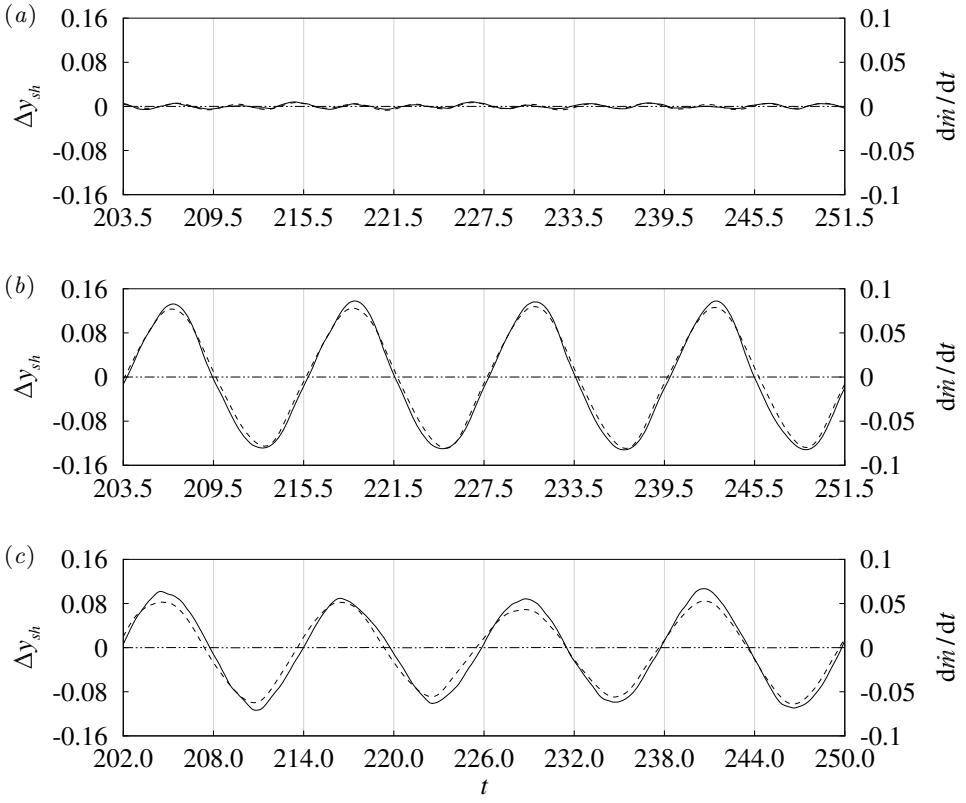

FIG. 14. Time histories of (- - -) $d\dot{m}_A/dt$, (-···-) $d\dot{m}_H/dt$ and (——) Δy_{sh} for (a) $\alpha = 90°$, (b) 60° and (c) 30°.

Figure 15 shows streamwise phase variations of the Q-criterion, $\Phi_Q(\boldsymbol{x}, f)$, across the cavity opening for both orthogonal and inclined cavities. The phase variations confirm the 2nd ($n = 2$) and 1st ($n = 1$) hydrodynamic modes present in the orthogonal and inclined cavities, respectively, which satisfy the phase condition $\Delta\Phi_Q(\boldsymbol{x}, f) = 2\pi n$, as detailed by Rockwell and Naudascher [83]. The plots also reveal that the hydrodynamic fluctuations near the upstream and downstream corners remain highly coherent with the wall pressure fluctuation at the base of the cavity ($\cos[\Phi_Q(\boldsymbol{x}, f) - \Phi_\chi(\boldsymbol{x}, f)] = 1$). This observation suggests that the phase of hydrodynamic cycle (e.g., from the initial formation to the final scattering of the vortex) is perfectly synchronised with the acoustic cycle (i.e., depthwise acoustic resonance), thereby creating a lock-in condition.

In order to examine the hydrodynamic field in more detail, a Fourier transform of Q-criterion is calculated and its magnitude at the resonance frequency is plotted in figure 16. This plot essentially reveals the zones of major vortical

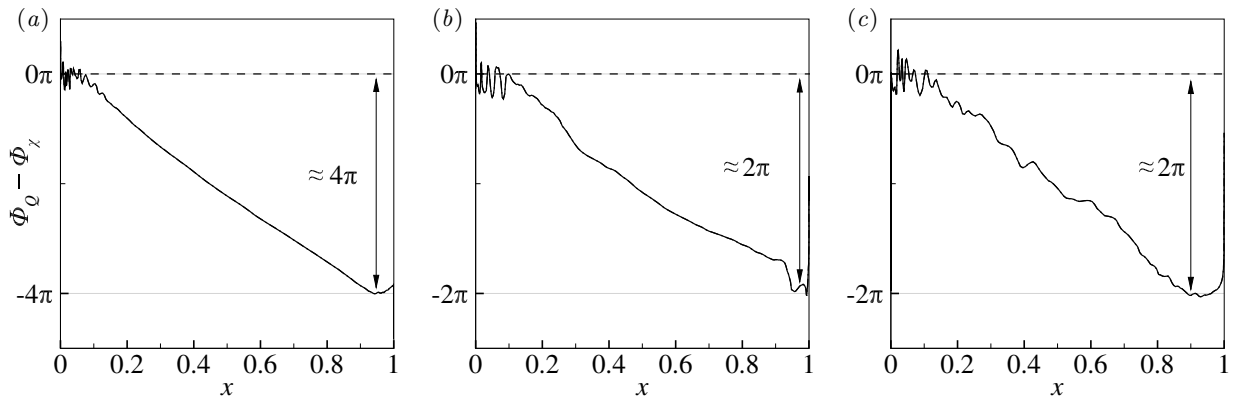

FIG. 15. The streamwise phase variation of the Fourier-transformed Q-criterion, $\Phi_Q(\boldsymbol{x}, f)$, measured across the cavity opening (i.e., at $y = 0$) at their respective tonal frequencies for (a) $\alpha = 90°$, (b) $60°$ and (c) $30°$. Note that the spatial variation of $\Phi_Q(\boldsymbol{x}, f)$ is calculated based on the phase reference of $\Phi_\chi(\boldsymbol{x}, f)$. Accordingly, the plots reveal regions of frequency modulation where the Q-Criterion fluctuation near the upstream and downstream corners remains highly synchronized with the averaged acoustic wall-pressure fluctuation at the cavity base ($\cos[\Phi_Q(\boldsymbol{x}, f) - \Phi_\chi(\boldsymbol{x}, f)] = 1$). This observation suggests that the phase of hydrodynamic cycle (e.g., initial vortex formation and subsequent impingement) is highly synchronized with the acoustic cycle (i.e., depthwise acoustic resonance).

activities contributing to the resonance cycle in each of the three cavity geometries. It is clear that the size of the zone is larger in the inclined cases as expected due to the larger vortex sizes visualised earlier. In the $\alpha = 60°$ case, the vortex is more intense and seemingly undergoes a noticeably undulated travel path. Meanwhile, the vortex generates less direct impingement at the downstream corner in the $\alpha = 60°$ case whereas the less intense vortex in the $\alpha = 30°$ case makes a more direct impingement. These balacing acts may have contributed to producing a similar sound level between the two cavities. However, it should be noted again that these observations are only based on the specific Fourier component at $St = 0.276$ and therefore do not represent the overall picture.

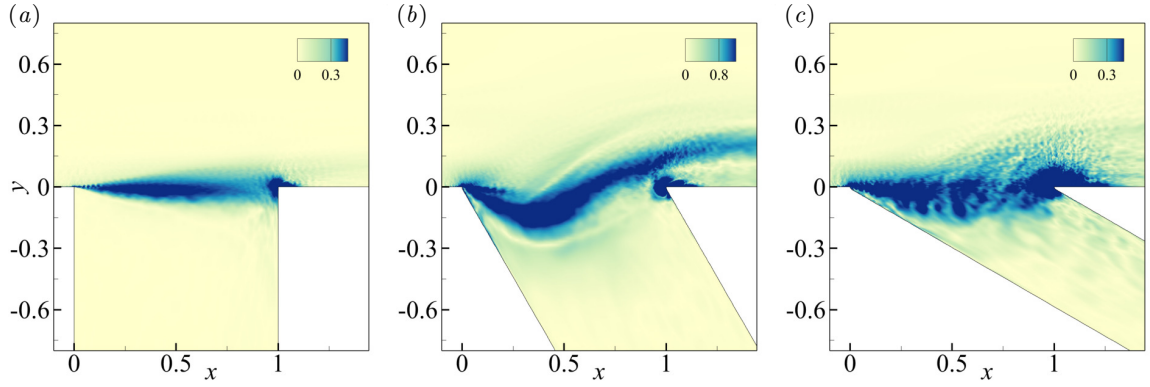

FIG. 16. The contour plots show the spatial distribution of the magnitude of Fourier-transformed Q-criterion, $|Q(\boldsymbol{x}, f)|$ at their respective tonal frequencies for (a) $\alpha = 90°$, (b) $60°$ and (c) $30°$.

We discussed earlier about the relatively slower travel speed of the large vortex in the inclined cavities in relation to the growth process of the vortex that is not particularly featured in the orthogonal cavity. In order to estimate the speed of the vortex travel, we look at the hydrodynamic component of the vertical momentum $(\rho v)_H$ fluctuating in space and time (across the cavity opening), presented in figure 17. We suggest that the spatio-temporal contour plot of $(\rho v)_H$ (which contains purely hydrodynamic fluctuations) displays the footprint of the large-scale vortex structure moving across the cavity opening. If we take an iso-contour line for $(\rho v)_H = 0$ (one of the white curves in figure 17) and calculate the slope of the curve, i.e. dx/dt as a function of x, it shows a representative speed of the vortex travel (u_V) at each point across the cavity opening ($x \in [0, 1]$ and $y = 0$). This is repeated for 10 consecutive curves of $(\rho v)_H = 0$ and an average is obtained. The resulting profiles of u_V are shown in figure 18. The results reveal that u_V is significantly lower in the inclined cavities than that of the orthogonal cavity across most of the cavity opening. It is apparent that the slower vortex travel of both inclined cavities occurs in two separate regions: 1) near

the upstream corner $x \in [0, 0.2]$ and 2) in the mid-to-downstream region $x \in [0.4, 0.9]$. We suggest that the former is linked with the initial roll-up of the vortex during the downward flapping of the shear layer, and the latter with the further growth of the vortex by entraining/merging adjacent eddies during the upward flapping of the shear layer. An additional observation here is that the inclined cavities, as a result of their unique vortex dynamics, produced thicker shear layers compared to the orthogonal cavity case, which is shown in figure 19. In this regard, an interesting study has been conducted recently by Mathias and Medeiros [84] who discussed the stability of cavity mixing/shear layers. They found that the most unstable mode frequency of a shear layer decreased as its thickness increased. This earlier study (although conducted for shallow and orthogonal cavities) supports the current explanation of the slower vortex travel possibly sustained by the lower-frequency instability of the thicker shear layer in the inclined cavities.

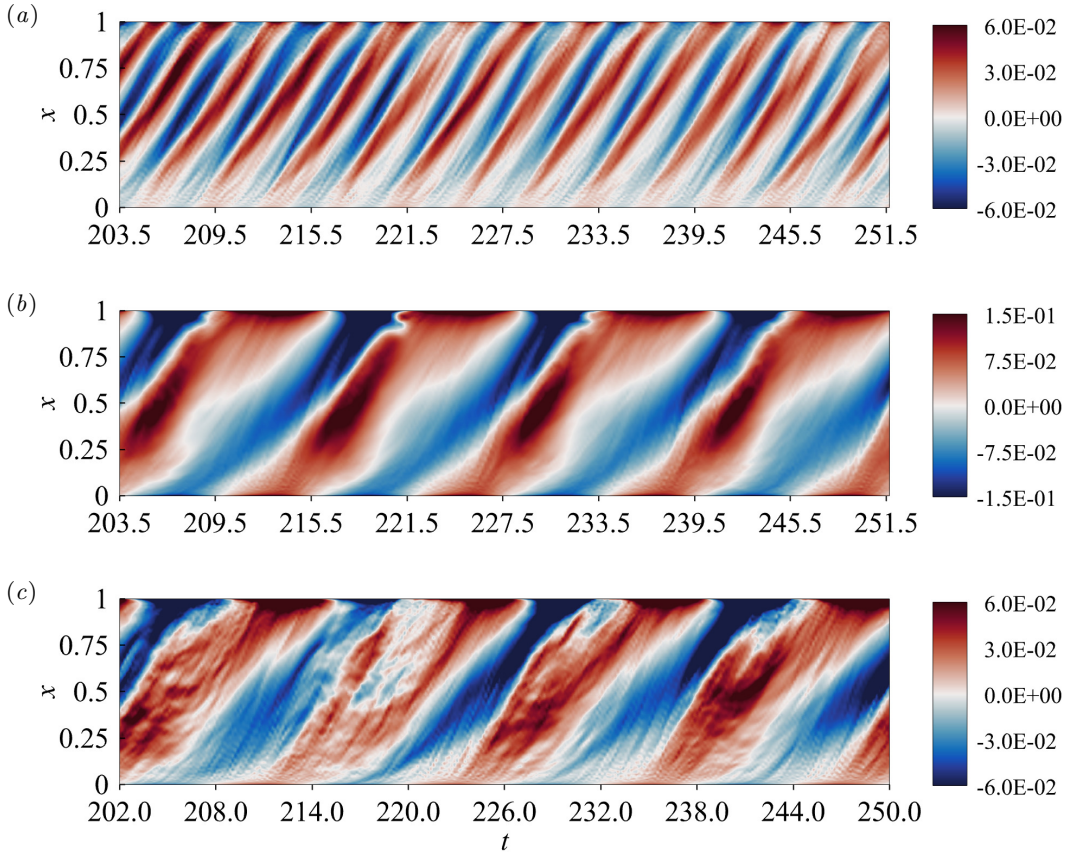

FIG. 17. Spatio-temporal contour plots of the hydrodynamic component of the vertical momentum $(\rho v)_H$ across the cavity opening ($y = 0$) for (a) $\alpha = 90°$, (b) $60°$ and (c) $30°$.

V. AEROACOUSTIC MODE AMPLIFICATIONS AND SELECTIONS

Section IV highlighted that the vortex dynamics plays a key role in determining the acoustic resonance mode and amplitude in deep and inclined cavities. Classical aeroacoustic theories that involve vortex dynamics [85, 86] suggest that instantaneous acoustic source power, Π, can be approximated using the following expression:

$$\Pi \approx -\rho_\infty \iint_{\boldsymbol{x}} (\boldsymbol{\omega} \times \boldsymbol{u}) \cdot \boldsymbol{u}_a \, d\boldsymbol{x}, \tag{31}$$

where $\boldsymbol{\omega}$ is the vorticity vector and $\boldsymbol{u}_a$ refers to the acoustic particle velocity vector. The triple-dot product $((\boldsymbol{\omega}\times\boldsymbol{u})\cdot\boldsymbol{u}_a)$ provides quantitative insight into the local energy transfer between the hydrodynamic and acoustic fields. In particular, the integrand captures the transfer of acoustic energy to hydrodynamic energy (e.g., $(\boldsymbol{\omega} \times \boldsymbol{u}) \cdot \boldsymbol{u}_a > 0$) and vice versa. For sustained oscillations to occur, it is important for the integral in Eq. (31) to remain positive over an acoustic cycle, ensuring that a favorable phase relationship between the Lamb vector $(\boldsymbol{\omega} \times \boldsymbol{u})$ and the acoustic field, $\boldsymbol{u}_a$. The

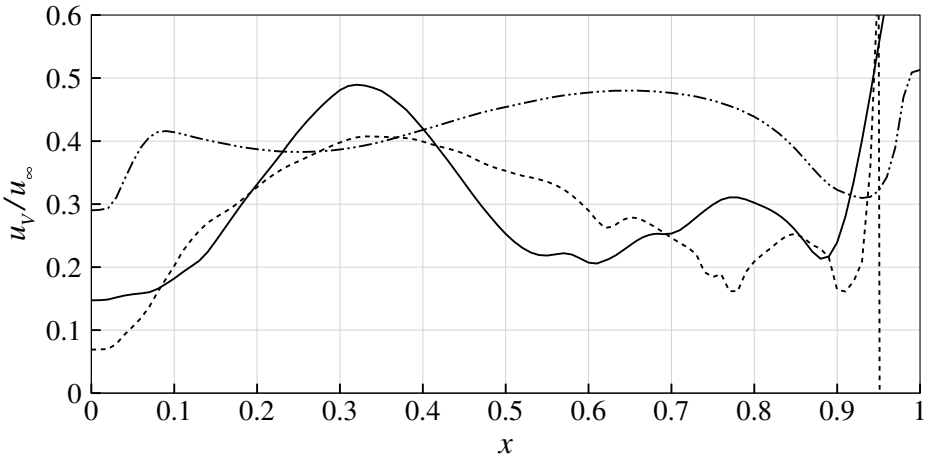

FIG. 18. Representative vortex travel speed u_V/u_∞ estimated for (-···-) $\alpha = 90°$, (——) 60° and (- - -) 30°. This estimation is based on iso-contour lines of $(\rho v)_H = 0$ in figure 17 from which $u_V = dx/dt$ is calculated.

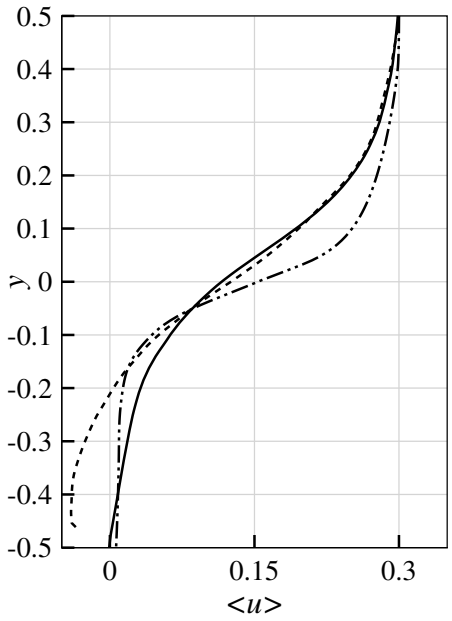

FIG. 19. Time-averaged profiles of streamwise velocity across the shear layer measured at $x = 0.8$ for (-···-) $\alpha = 90°$, (——) 60° and (- - -) 30°, displaying thicker shear layers produced in the inclined cavities compared to the orthogonal case.

following discussion further examines this energy exchange process by analyzing the temporal dynamics of the Lamb vector within resonant acoustic fields in inclined cavities.

Figure 20 shows the time evolution of the Lamb vector and the acoustic particle velocity field in an $\alpha = 30°$ inclined cavity over an acoustic cycle. The acoustic absorption phase is depicted in figures 20(a,b), where hydrodynamic instabilities within the shear-layer absorb acoustic energy to form a coherent vortex near the upstream corner, while the residual vorticity near the downstream corner from the preceding cycle also contributes to this absorption. The second half of the acoustic production phase is captured in figures 20(c,d), where the vorticity-dominated regions are now in phase with the acoustic particle velocity field until their ejection from the cavity in the same direction as the acoustic particle velocity. Subsequently, figure 21 shows the time evolution of the Lamb vector and the acoustic particle velocity field in the $\alpha = 60°$ inclined cavity over an similar acoustic cycle. Although there are significant similarities with the $\alpha = 30°$ inclined cavity, two key differences are observed. First, the vortex structure in the $\alpha = 60°$ inclined cavity exhibits enhanced spanwise coherence, contributing to a more pronounced Lamb vector and consequently enhanced instantaneous acoustic source power, according to Eq. (31). Second, the diminished residual

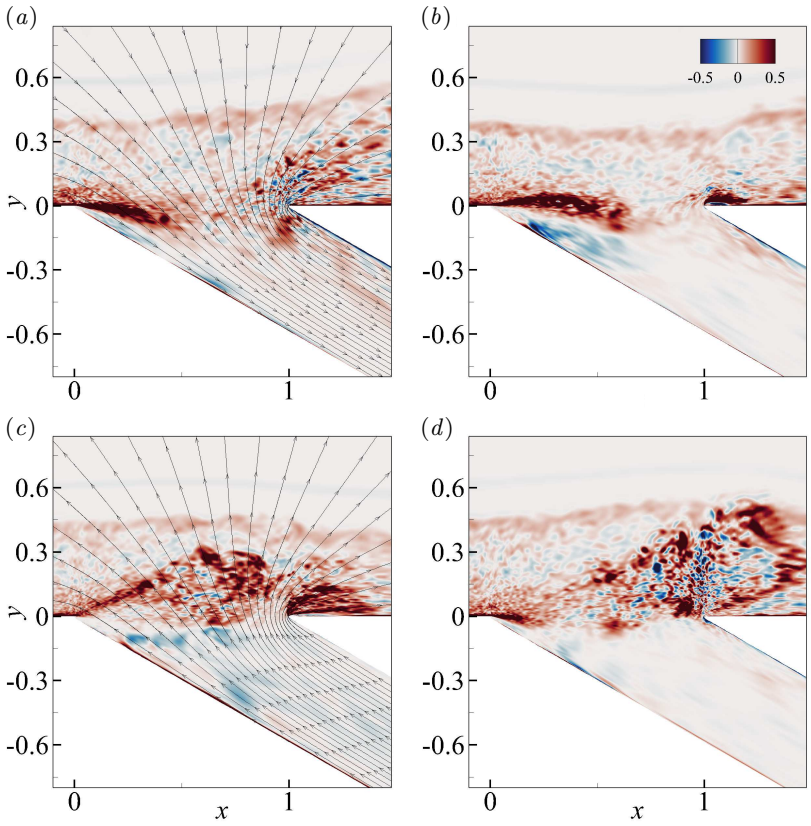

FIG. 20. The time evolution of the Lamb vector ($\boldsymbol{\omega} \times \boldsymbol{u}$) in the vertical direction for the $\alpha = 30^\circ$ inclined cavity is examined for a single acoustic cycle. The contour plots capture two key time instants: those (a) when the instantaneous acoustic source power Π reaches its minimum and (c) when it reaches its maximum. The plots (b) and (d) indicate the time junctures when the instantaneous acoustic source power becomes zero, such as when $\Pi = 0$. Here, the superimposed streamline represents the instantaneous acoustic particle velocity field.

vorticity near the downstream corner in the $\alpha = 60^\circ$ inclined cavity reduces the overall absorption of acoustic energy. These factors may potentially explain the stronger acoustic response observed in the $\alpha = 60^\circ$ inclined cavity.

The preceding discussion qualitatively explains the intense acoustic response observed in inclined cavities. To further investigate the fundamental mechanisms driving noise amplification in these cavity flow systems, an APE-resolvent analysis, as outlined in Subsection II D, has been conducted. The primary objective of this analysis is to establish a direct quantitative relationship between the Lamb vector and the magnitude of the acoustic response by examining the corresponding amplification rates and the forcing-response mode shapes of the APE-resolvent operator. Accordingly, figure 22 presents the three leading amplification rates of the APE-resolvent operator across various frequencies. The results reveal that the leading amplification rate is significantly higher than the second and third rates at tonal frequencies across all cavity inclinations, underscoring the low-rank nature of the cavity oscillations examined in this study. Subsequently, this low-rank behavior justifies a rank-1 approximation of the APE-resolvent operator, where the dominant leading mode alone sufficiently characterizes the cavity system's acoustic response. Specifically,

$$\boldsymbol{R}(\bar{q};\omega) = \hat{\boldsymbol{U}}\boldsymbol{\Sigma}\hat{\boldsymbol{V}}^H = \sum_i \sigma_i \boldsymbol{u}_i \boldsymbol{v}_i^H \approx \sigma_1 \boldsymbol{u}_1 \boldsymbol{v}_1^H, \tag{32}$$

where $\boldsymbol{u}_1$ and $\boldsymbol{v}_1$ represent the leading forcing and response modes, respectively, while σ_1 denotes the gain of the leading forcing-response pair. The superscript H in Eq. (32) refers to the Hermitian transpose operation. Note that the response and forcing mode shapes are obtained from singular value decomposition, through which the leading mode shapes are normalized by construction such that $||\boldsymbol{u}_1|| = ||\boldsymbol{v}_1|| = 1$. Consequently, this approximation establishes a quantitative connection between the input forcing, $\hat{\boldsymbol{f}}_\omega$ (e.g., the Lamb vector), and the corresponding output acoustic field quantities, $\hat{\boldsymbol{q}}_\omega$ (e.g., the acoustic pressure fluctuations), which can be represented as

$$\hat{\boldsymbol{q}}_\omega = \boldsymbol{R}(\bar{q};\omega)\hat{\boldsymbol{f}}_\omega \approx \sigma_1 \boldsymbol{u}_1 \boldsymbol{v}_1^H \hat{\boldsymbol{f}}_\omega = \sigma_1 \boldsymbol{u}_1 \sum_j v_{1,j}^* \hat{f}_{\omega,j} = \sigma_1 \boldsymbol{u}_1 F_\omega, \tag{33}$$

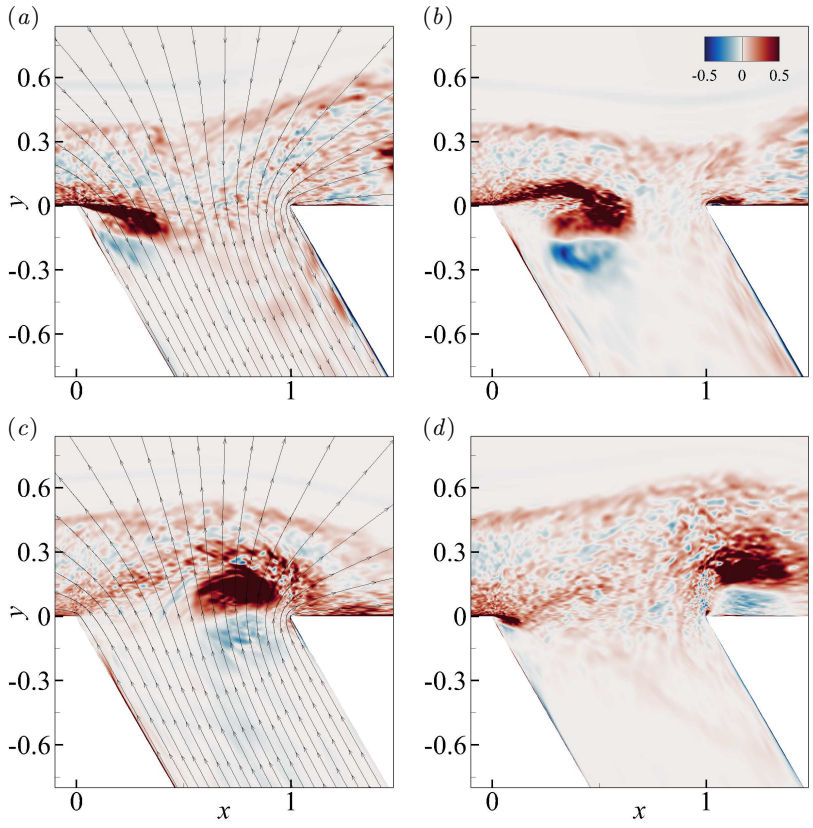

FIG. 21. The time evolution of the Lamb vector ($\boldsymbol{\omega} \times \boldsymbol{u}$) in the vertical direction for the $\alpha = 60^{\circ}$ inclined cavity is examined for a single acoustic cycle. The contour plots capture two key time instants: those (a) when the instantaneous acoustic source power, Π, reaches its minimum, and (c) when it reaches its maximum. The plots (b) and (d) indicate the time junctures when the instantaneous acoustic source power becomes zero, such as when $\Pi = 0$. Here, the superimposed streamline represents the instantaneous acoustic particle velocity field.

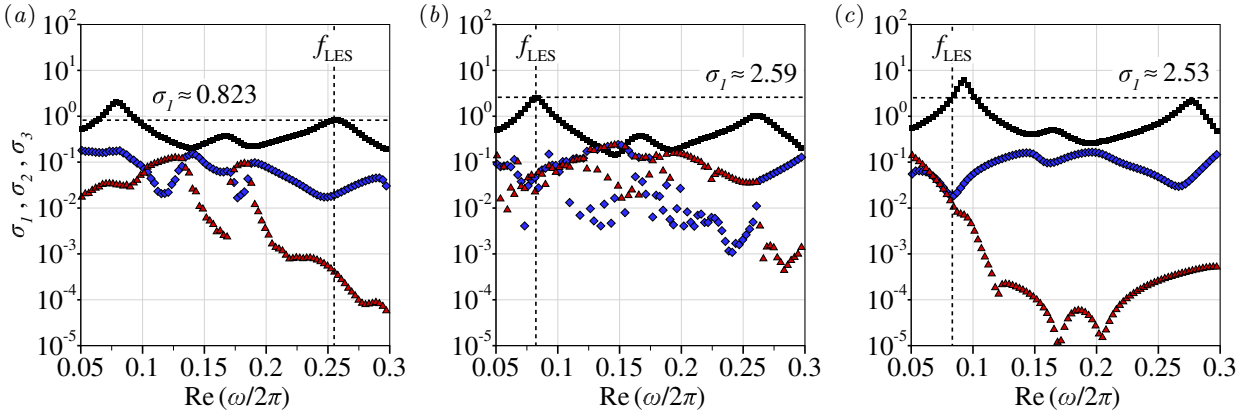

FIG. 22. The low-rank behavior of the APE-resolvent operator is visualized through the first three leading magnification rates: (■) σ_1, (◆) σ_2 and (▲) σ_3 for (a) $\alpha = 90^{\circ}$, (b) 60° and (c) 30°. The vertical dashed line (- - -) indicates the tonal frequency observed in the LES, while the horizontal dashed line (- - -) represents the leading amplification rate σ_1 corresponding to that frequency.

where the index "j" denotes the grid points. Here, the measure of the source and sink is the correlation between the leading hydrodynamic forcing ($\hat{f}_{\omega,j}$) and the acoustic response ($v^*_{1,j}$), i.e. $v^*_{1,j}\hat{f}_{\omega,j}$ at a given point in space (j). If the correlation is positive (in either of the x- or $y-$direction), the location can be regarded as a source region ($v^*_{1,j}\hat{f}_{\omega,j} > 0$), and if negative, a sink region ($v^*_{1,j}\hat{f}_{\omega,j} < 0$). Meanwhile, $F_\omega = \boldsymbol{v}_1^H \hat{\boldsymbol{f}}_\omega = \boldsymbol{v}_1^* \cdot \hat{\boldsymbol{f}}_\omega$ is the sum of all

sources and sinks. Figure 23 presents the spatial distribution of the reconstructed acoustic pressure field calculated using Eq. (33), which shows strong agreement with the LES data, thereby reconfirming the suitability of the rank-1 approximation for capturing the dominant acoustic response of cavity flows examined in this study.

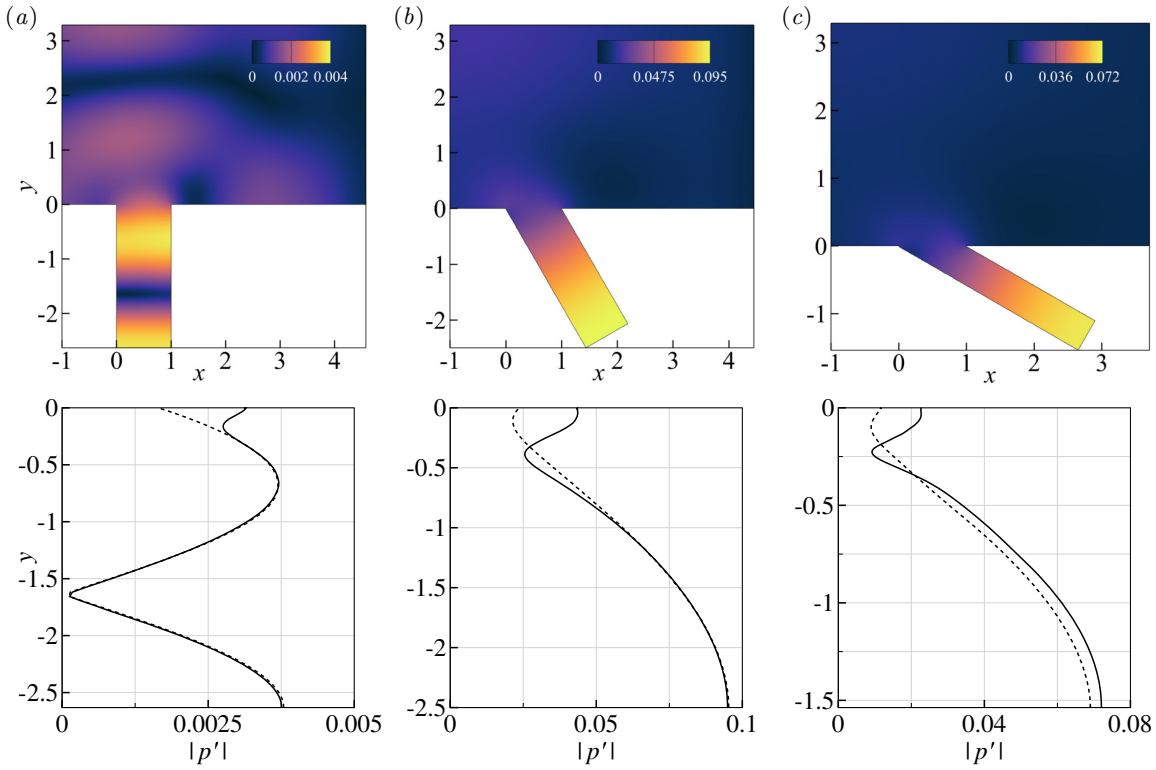

FIG. 23. The first row of contour plots shows the spatial distribution of the magnitude of the reconstructed acoustic pressure field $|p'_{\mathrm{APE}}|$ for (a) $\alpha = 90°$, (b) $60°$ and (c) $30°$. The second row of line plots the depthwise distribution of wall-pressure fluctuations measured along the upstream cavity wall ($x = 0$) from the (——) LES in comparison with the (- - -) rank-1 approximation computed using Eq. (33).

Figure 24 provides some useful information showing that factors like σ_1 and F_ω obtained from the APE-resolvent operator correlate well with the sound pressure levels directly observed from the current LES (p'_{LES}) for different cavity inclinations. First, the leading gains are higher in the inclined cavities since they are driven by the 1st depthwise acoustic modes which have smaller radiation losses (more perturbation energy contained within the cavity) that those of the orthogonal cavity as previously discussed from figure 9(b). Second, the sum of all sources and sinks (in

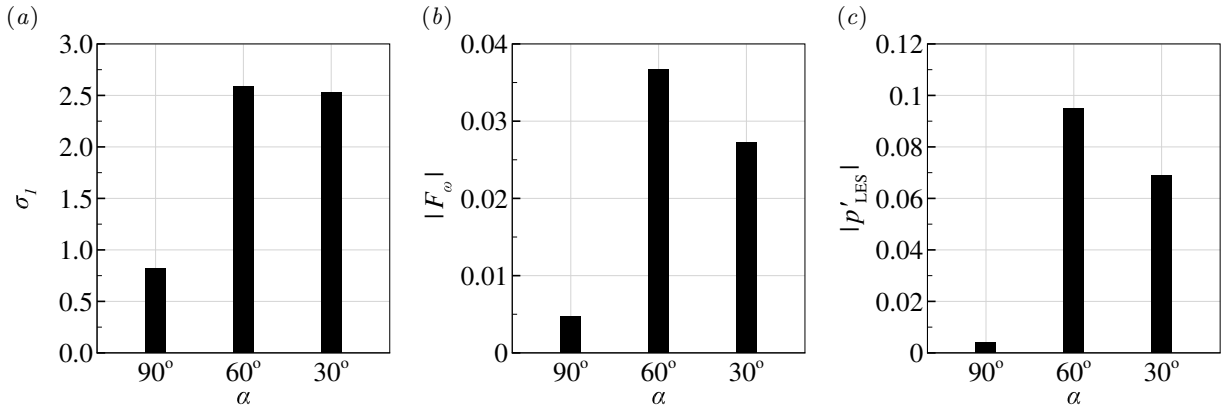

FIG. 24. Histogram plots showing (a) the first leading gain of the APE-resolvent operator σ_1; (b) the sum of sources and sinks (magnitude) $|F_\omega|$; and, (c) the magnitude of the acoustic pressure $|p'_{\mathrm{LES}}|$, for three different cavity inclinations.

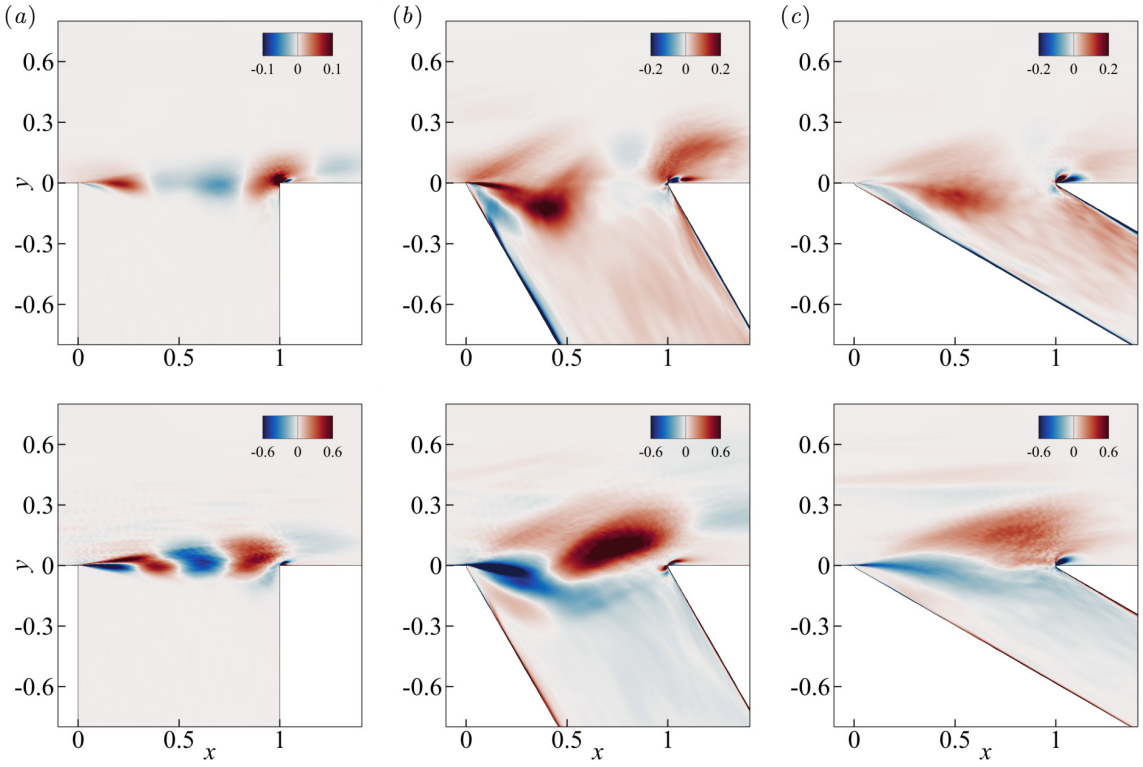

FIG. 25. The spatial distribution of the real part of $\boldsymbol{v}_1^* \odot \hat{\boldsymbol{f}}_\omega$ in the streamwise direction (top panels) and vertical direction (bottom panels) for (a) $\alpha = 90°$, (b) $60°$ and (c) $30°$. Here, the sources and sinks are represented by regions where $\boldsymbol{v}_1^* \odot \hat{\boldsymbol{f}}_\omega > \boldsymbol{0}$ and $\boldsymbol{v}_1^* \odot \hat{\boldsymbol{f}}_\omega < \boldsymbol{0}$, respectively. The phase of the plots is selected such that the imaginary part of F_ω is zero.

magnitude) appears also greater in the inclined cavities. On the other hand, the orthogonal cavity seems to suffer a significant source-sink cancellation effect, perhaps related to the higher hydrodynamic and acoustic modes that prevailed. Figure 25(a) shows source ($v_{1,j}^* \hat{f}_{\omega,j} > 0$) and sink regions ($v_{1,j}^* \hat{f}_{\omega,j} < 0$) in the orthogonal cavity case where the two opposite regions have an almost equal size and magnitude leading to a mutual cancellation. In contrast, the inclined cavities exhibit unequal sizes of the source and sink regions indicating less effective cancellation between the two, as shown in figures 25(b) and (c). This may have contributed to amplifying the sound pressure level, also with the help of the minimal radiation losses in the 1st depthwise acoustic mode that prevailed in the inclined cavities.

Thus far, the discussions have primarily centered on elucidating the aeroacoustic characteristics of cavity oscillations, with limited emphasis on the influence of incoming flow properties. To address this gap, we leverage insights from the acoustic particle velocity analysis across varying pulsation levels, as discussed in Section III, to assess the impact of acoustic forcing near the upstream corner on the cavity oscillation frequency. Here, the effect of acoustic forcing is quantified by evaluating the peak acoustic particle displacement induced by depthwise acoustic resonance, expressed as

$$\theta_a = \frac{|p'|}{\rho_\infty a_\infty 2\pi He}, \tag{34}$$

where $|p'|$ denotes the magnitude of the Fourier-transformed pressure fluctuations measured at the cavity base, and He represents the peak Helmholtz number identified in the pressure spectra of the LES results. According to Bagwell [87], lock-in oscillations may occur when the acoustic particle displacement is on the same order of magnitude as the momentum thickness. Subsequently, we compare our LES data with previous experimental findings on deep cavity flows to provide further insight into the relationship between acoustic forcing and cavity oscillation dynamics.

Figure 26 presents the ratios of acoustic particle displacement to momentum thickness (θ_a/θ) as a function of the peak Strouhal number collected from previous experimental data and the authors' computational work. The plot reveals three distinct flow-acoustic resonance regimes, i.e. a low-, mid- and high-frequency regimes centred around $St \sim 0.27$, 0.4 and 0.85, respectively. Note that all the cases in the plot except the current ones are from orthogonal deep cavities. What is intriguing in this plot is that there is one experimental case found from Yang et al. [9] which occurred at $St = 0.27$ (as is with the current inclined cavities) even though it came from an orthogonal cavity. Yang

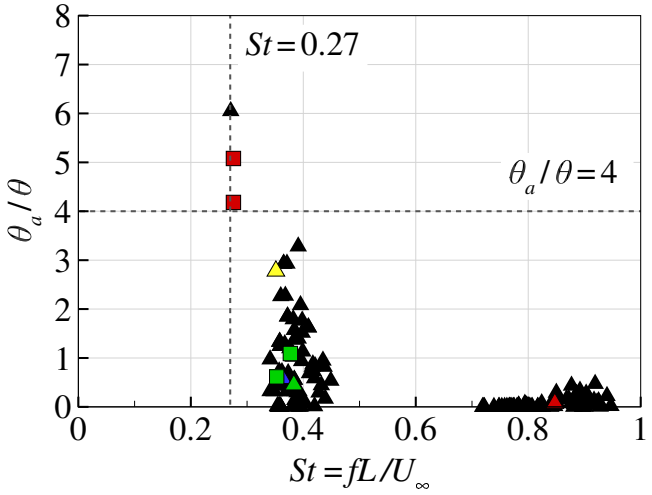

FIG. 26. The scatter plot shows the ratio of acoustic particle displacement θ_a to the momentum thickness θ at three distinct flow-acoustic resonance regimes. Different symbol colors represent data from various studies on orthogonal cavity flows: (▲) Yang et al. [9], (△) Bagwell [87], (▲) Forestier et al. [88], (△) Ho and Kim [23], and (▲) represents the current LES result at $M_\infty = 0.3$. The current LES results for inclined cavities at (■) $M_\infty = 0.2$ and (■) 0.3 are provided. For fair comparison with experimental studies, the momentum thickness θ is measured at 10% away from the upstream cavity corner, and the values for each cavity case are provided in Table I. The horizontal line suggests that the ratio between acoustic particle displacement and momentum thickness ($\theta_a/\theta \geq 4$) may serve as an indicator for predicting the onset of amplified resonance at $St = 0.27$.

et al. reported it as an unexpected and intense cavity resonance mode referred to as "$h1{*}a1$". Despite the scarcity of data around $St \sim 0.27$, we can see a convincing trend present in the plot that a higher value of θ_a/θ is required to produce a resonance at a lower frequency mode. Although it is premature to draw a conclusion with the small number of samples available to date, the authors suggest that a threshold condition $\theta_a/\theta > 4$ may be used to predict a low-frequency deep-cavity resonance at $St \sim 0.27$.

VI. CONCLUDING REMARKS

We investigated the aeroacoustic behavior of deep cavities with an aspect ratio of $D/L = 2.632$ and three different inclination angles ($\alpha = 30°$, 60°, and 90°) at two different Mach numbers ($M_\infty = 0.2$ and 0.3) using wall-resolved large-eddy simulations. The inclined cavities at $M_\infty = 0.3$ generated unexpected acoustic responses with peak amplitudes nearly 30 dB higher than those observed with the orthogonal cavity. Moreover, the peak frequency ($St = 0.276$) was significantly lower compared to the orthogonal case ($St = 0.849$). This was not predicted by Rossiter's model that accounts for streamwise feedback mechanism only. Various analysis methods were used to investigate responsible physical mechanisms that generated the unexpected results from the inclined cavities. For the orthogonal cavity, a lock-in event occurred between the 2nd depthwise acoustic mode ($He \approx 0.255$) and the 2nd hydrodynamic mode ($St = 0.849$) which exhibited two small vortices travelling across the cavity opening simultaneously. Coincidentally, this frequency also matched Rossiter's prediction with $St_n = (n - 1/4)/(M_\infty + 1/\kappa)$ where $n = 2$ and $\kappa = 0.57$. In contrast, the inclined cavities resulted in a lock-in between the 1st depthwise acoustic mode ($He = 0.083$) and the 1st hydrodynamic mode ($St = 0.276$) which the Rossiter's model did not predict. The 1st hydrodynamic mode which involves only one vortex across the cavity opening was due to a significantly different vortex dynamics produced in the inclined cavities. The identified vortex dynamics consists of a pronounced Kelvin-Helmholtz instability in the shear layer that produces a roll-up vortex that spends a substantial amount of time growing by merging smaller eddies rather than consistently travelling downstream. This process slowed the overall vortex convection speed and prolonged the vortex dwell time, ultimately resulting in a lower resonance frequency (a lock-in with the 1st acoustic mode). Additionally, due to the large size, only a single vortex occupied the cavity opening.

We suggested that the enhanced level of Kelvin-Helmholtz instability appeared in the inclined cavities was linked with the low level of radiation losses identified through the APE eigenmode analysis. The smaller radiation loss (in comparison to the orthogonal cavity case) means that more acoustic perturbation energy is contained within the cavity which may have elevated the shear-layer flapping. This effect was also quantified by tracing the change of mass flow rate across the cavity opening and also the streamline displacement. Meanwhile, the APE-resolvent analysis displayed

the source and sink regions in each cavity, from which we found that the source-sink cancellation was less pronounced in the inclined cavities. These factors contributed to the enhanced amplitude of resonance present in the inclined cavities. Finally, we hypothesized that the ratio between the acoustic particle displacement and the momentum thickness $\theta_a/\theta > 4$ might be a necessary condition for the onset of the low-frequency resonance ($St \sim 0.27$) in deep and inclined cavities.

While the current study provides valuable insights into flow-acoustic resonances in deep and inclined cavity configurations, it has certain limitations that warrant further research. Firstly, the findings are specific to the aspect ratio of $L/D = 2.632$ and the Mach numbers of 0.2 and 0.3 considered in this study. Further investigations are required to better understand the distinctive vortex dynamics and the low-frequency mode selection process across various aspect ratios and over a broader range of Mach and Reynolds numbers. Secondly, since this study focused on a two-dimensional cavity geometry, the effects of three-dimensional geometries such as cavities with a finite span or circular cross-sections with various inclinations are entirely unknown. Additionally, different cavity floor configurations (e.g., non-orthogonal to the side walls and/or non-planar) may influence resonance frequencies and amplitudes. Finally, future studies should explore optimal cavity geometries and/or flow conditions that may lead to strategies for mitigating or controlling deep cavity resonance, given the significant practical implications for various engineering applications.

ACKNOWLEDGMENTS

The authors would like to acknowledge the studentship provided by Rolls-Royce UTC (University Technology Centre) for Propulsion Systems Noise at the University of Southampton. The authors also thank EPSRC (Engineering and Physical Sciences Research Council) for the computational time made available on the UK supercomputing facility ARCHER2 via the UK Turbulence Consortium (EP/R029326/1).

[1] J. T. Coffman and M. D. Bernstein, Failure of safety valves due to flow-induced vibration, Journal of Pressure Vessel Technology **102**, 112 (1980).
[2] D. Galbally, G. García, J. Hernando, J. de Dios Sánchez, and M. Barral, Analysis of pressure oscillations and safety relief valve vibrations in the main steam system of a boiling water reactor, Nuclear Engineering and Design **293**, 258 (2015).
[3] J. C. Bruggeman, A. Hirschberg, M. E. H. van Dongen, A. P. J. Wijnands, and J. Gorter, Flow induced pulsations in gas transport systems: Analysis of the influence of closed side branches, Journal of Fluids Engineering **111**, 484 (1989).
[4] S. Ziada, Flow-excited acoustic resonance in industry, Journal of Pressure Vessel Technology **132** (2010).
[5] S. Ziada, A. Oengören, and A. Vogel, Acoustic resonance in the inlet scroll of a turbo-compressor, Journal of Fluids and structures **16**, 361 (2002).
[6] A. A. Aleksentsev, A. N. Sazhenkov, and S. V. Sukhinin, Acoustic resonance phenomena in air bleed channels in aviation engines, Journal of Applied Mechanics and Technical Physics **57**, 971 (2016).
[7] C. Perrot-Minot, E. Mignot, R. Perkins, D. Lopez, and N. Riviere, Vortex shedding frequency in open-channel lateral cavity, Journal of Fluid Mechanics **892** (2020).
[8] M. C. A. M. Peters, *Aeroacoustic sources in internal flows* (Eindhoven University of Technology, 1993).
[9] Y. Yang, D. Rockwell, K. L. F. Cody, and M. Pollack, Generation of tones due to flow past a deep cavity: Effect of streamwise length, Journal of Fluids and Structures **25**, 364 (2009).
[10] J. E. Rossiter, *Wind tunnel experiments on the flow over rectangular cavities at subsonic and transonic speeds*, Tech. Rep. (Ministry of Aviation; Royal Aircraft Establishment; RAE Farnborough, 1964).
[11] C. W. Rowley and D. R. Williams, Dynamics and control of high-reynolds-number flow over open cavities, Annu. Rev. Fluid Mech. **38**, 251 (2006).
[12] K. Karamcheti, Acoustic radiation from two-dimensional rectangular cut-outs in aerodynamic surfaces, NACA TN **3487** (1955).
[13] H. E. Plumblee, J. S. Gibson, and L. W. Lassiter, *A theoretical and experimental investigation of the acoustic response of cavities in an aerodynamic flow*, Tech. Rep. (Lockheed Aircraft Corp Marietta GA, 1962).
[14] L. F. East, Aerodynamically induced resonance in rectangular cavities, Journal of Sound and Vibration **3**, 277 (1966).
[15] D. Rockwell and E. Naudascher, Review—self-sustaining oscillations of flow past cavities, Journal of Fluids Engineering **100**, 152 (1978).
[16] W. Koch, Acoustic resonances in rectangular open cavities, AIAA Journal **43**, 2342 (2005).
[17] C. K. W. Tam, Excitation of instability waves in a two-dimensional shear layer by sound, Journal of Fluid Mechanics **89**, 357 (1978).
[18] D. Tonon, A. Hirschberg, J. Golliard, and S. Ziada, Aeroacoustics of pipe systems with closed branches, International Journal of Aeroacoustics **10**, 201 (2011).

[19] S. Ziada and P. Lafon, Flow-excited acoustic resonance excitation mechanism, design guidelines, and counter measures, Applied Mechanics Reviews **66** (2014).

[20] E. Tinar and D. Rockwell, Generation of locked-on flow tones: Effect of damping, Journal of Fluids and Structures **44**, 129 (2014).

[21] C. W. Rowley, T. Colonius, and A. J. Basu, On self-sustained oscillations in two-dimensional compressible flow over rectangular cavities, Journal of Fluid Mechanics **455**, 315 (2002).

[22] B. A. Tuna and D. Rockwell, Self-sustained oscillations of shallow flow past sequential cavities, Journal of Fluid Mechanics **758**, 655 (2014).

[23] Y. W. Ho and J. W. Kim, A wall-resolved large-eddy simulation of deep cavity flow in acoustic resonance, Journal of Fluid Mechanics **917** (2021).

[24] S. Ziada, A flow visualization study of flow-acoustic coupling at the mouth of a resonant side-branch, Journal of Fluids and Structures **8**, 391 (1994).

[25] S. Dequand, S. Hulshoff, and A. Hirschberg, Self-sustained oscillations in a closed side branch system, Journal of Sound and Vibration **265**, 359 (2003).

[26] R. Bravo, S. Ziada, and M. Dokainish, Aeroacoustic response of an annular duct with coaxial closed side branches, in *11th AIAA/CEAS Aeroacoustics Conference* (2005) p. 3019.

[27] V. Theofilis, Globally unstable basic flows in open cavities, in *6th Aeroacoustics Conference and Exhibit* (2000) p. 1965.

[28] F. Giannetti and P. Luchini, Structural sensitivity of the first instability of the cylinder wake, Journal of Fluid Mechanics **581**, 167 (2007).

[29] G. A. Bres and T. Colonius, Three-dimensional instabilities in compressible flow over open cavities, Journal of Fluid Mechanics **599**, 309 (2008).

[30] V. Theofilis, Global linear instability, Annual Review of Fluid Mechanics **43**, 319 (2011).

[31] S. Yamouni, D. Sipp, and L. Jacquin, Interaction between feedback aeroacoustic and acoustic resonance mechanisms in a cavity flow: a global stability analysis, Journal of Fluid Mechanics **717**, 134 (2013).

[32] P. J. Schmid and L. Brandt, Analysis of Fluid Systems: Stability, Receptivity, Sensitivity: Lecture notes from the FLOW-NORDITA Summer School on Advanced Instability Methods for Complex Flows, Stockholm, Sweden, 2013, Applied Mechanics Reviews **66** (2014), 024803.

[33] F. Meseguer-Garrido, J. D. Vicente, E. Valero, and V. Theofilis, On linear instability mechanisms in incompressible open cavity flow, Journal of Fluid Mechanics **752**, 219 (2014).

[34] V. Citro, F. Giannetti, L. Brandt, and P. Luchini, Linear three-dimensional global and asymptotic stability analysis of incompressible open cavity flow, Journal of Fluid Mechanics **768**, 113 (2015).

[35] O. Marquet and L. Lesshafft, Identifying the active flow regions that drive linear and nonlinear instabilities, arXiv preprint arXiv:1508.07620 (2015).

[36] Q. Liu, F. Gómez, and V. Theofilis, Linear instability analysis of low-incompressible flow over a long rectangular finite-span open cavity, Journal of Fluid Mechanics **799**, R2 (2016).

[37] Y. Sun, K. Taira, L. N. Cattafesta, and L. S. Ukeiley, Biglobal instabilities of compressible open-cavity flows, Journal of Fluid Mechanics **826**, 270 (2017).

[38] J. M. Chomaz, Global instabilities in spatially developing flows: non-normality and nonlinearity, Annu. Rev. Fluid Mech. **37**, 357 (2005).

[39] L. N. Trefethen, A. E. Trefethen, S. C. Reddy, and T. A. Driscoll, Hydrodynamic stability without eigenvalues, Science **261**, 578 (1993).

[40] B. J. McKeon and A. S. Sharma, A critical-layer framework for turbulent pipe flow, Journal of Fluid Mechanics **658**, 336 (2010).

[41] Y. Sun, Q. Liu, L. N. Cattafesta III, L. S. Ukeiley, and K. Taira, Resolvent analysis of compressible laminar and turbulent cavity flows, AIAA journal **58**, 1046 (2020).

[42] Q. Liu, Y. Sun, C.-A. Yeh, L. S. Ukeiley, L. N. Cattafesta, and K. Taira, Unsteady control of supersonic turbulent cavity flow based on resolvent analysis, Journal of Fluid Mechanics **925** (2021).

[43] Q. Liu and D. Gaitonde, Acoustic response of turbulent cavity flow using resolvent analysis, Physics of Fluids **33** (2021).

[44] E. Boujo, M. Bauerheim, and N. Noiray, Saturation of a turbulent mixing layer over a cavity: response to harmonic forcing around mean flows, Journal of Fluid Mechanics **853**, 386 (2018).

[45] L. Larchevêque, P. Sagaut, I. Mary, O. Labbé, and P. Comte, Large-eddy simulation of a compressible flow past a deep cavity, Physics of Fluids **15**, 193 (2003).

[46] B. Thornber and D. Drikakis, Implicit large-eddy simulation of a deep cavity using high-resolution methods, AIAA journal **46**, 2634 (2008).

[47] P. Sampath and K. P. Sinhamahapatra, Numerical analysis of characteristic features of shallow and deep cavity in supersonic flow, International Journal of Computational Fluid Dynamics **30**, 231 (2016).

[48] Z. Chen and N. A. Adams, Mode interactions of a high-subsonic deep cavity, Physics of Fluids **29** (2017).

[49] T. Pedergnana, C. Bourquard, A. Faure-Beaulieu, and N. Noiray, Modeling the nonlinear aeroacoustic response of a harmonically forced side branch aperture under turbulent grazing flow, Physical Review Fluids **6**, 023903 (2021).

[50] J. W. Kim, High-order compact filters with variable cut-off wavenumber and stable boundary treatment, Comput. Fluids **39**, 1168 (2010).

[51] D. J. Garmann, M. R. Visbal, and P. D. Orkwis, Comparative study of implicit and subgrid-scale model large-eddy simulation techniques for low-reynolds number airfoil applications, International Journal for Numerical Methods in Fluids **71**, 1546 (2012).

[52] F. M. White, Viscous fluid flow 2nd edition mcgraw-hill, New York (1991).
[53] J. W. Kim and P. J. Morris, Computation of subsonic inviscid flow past a cone using high-order schemes, AIAA J. **40**, 1961 (2002).
[54] J. W. Kim, A. S. H. Lau, and N. D. Sandham, CAA boundary conditions for airfoil noise due to high-frequency gusts, Proc. Eng. **6**, 244 (2010).
[55] J. W. Kim, A. S. H. Lau, and N. D. Sandham, Proposed boundary conditions for gust-airfoil interaction noise, AIAA J. **48**, 2705 (2010).
[56] J. W. Kim, Optimised boundary compact finite difference schemes for computational aeroacoustics, J. Comput. Phys. **225**, 995 (2007).
[57] J. W. Kim and D. J. Lee, Generalized characteristic boundary conditions for computational aeroacoustics, AIAA J. **38**, 2040 (2000).
[58] J. W. Kim and D. J. Lee, Generalized characteristic boundary conditions for computational aeroacoustics, part 2, AIAA J. **42**, 47 (2004).
[59] J. W. Kim, Quasi-disjoint pentadiagonal matrix systems for the parallelization of compact finite-difference schemes and filters, J. Comput. Phys. **241**, 168 (2013).
[60] T. Y. Na and Y. P. Lu, Turbulent flow development characteristics in channel inlets, Applied Scientific Research **27**, 425 (1973).
[61] D. B. Spalding, A single formula for the "law of the wall", Journal of Applied Mechanics **28**, 455 (1961).
[62] A. Lozano-Durán and J. Jiménez, Effect of the computational domain on direct simulations of turbulent channels up to $Re_\tau = 4200$, Physics of Fluids **26** (2014).
[63] M. E. Goldstein, *Aeroacoustics* (McGraw-Hill, 1976) pp. 54–59.
[64] R. Ewert and W. Schröder, Acoustic perturbation equations based on flow decomposition via source filtering, Journal of Computational Physics **188**, 365 (2003).
[65] K. Aly and S. Ziada, Effect of mean flow on the trapped modes of internal cavities, Journal of Fluids and Structures **33**, 70 (2012).
[66] N. Arya and A. De, Effect of vortex and entropy sources in sound generation for compressible cavity flow, Physics of Fluids **33**, 046107 (2021).
[67] K. W. Thompson, Time dependent boundary conditions for hyperbolic systems, Journal of Computational Physics **68**, 1 (1987).
[68] K. W. Thompson, Time-dependent boundary conditions for hyperbolic systems, II, Journal of Computational Physics **89**, 439 (1990).
[69] G. W. Stewart, A krylov–schur algorithm for large eigenproblems, SIAM Journal on Matrix Analysis and Applications **23**, 601 (2002).
[70] P. E. Doak, Momentum potential theory of energy flux carried by momentum fluctuations, Journal of Sound and Vibration **131**, 67 (1989).
[71] S. Unnikrishnan and D. V. Gaitonde, Acoustic, hydrodynamic and thermal modes in a supersonic cold jet, Journal of Fluid Mechanics **800**, 387 (2016).
[72] S. Unnikrishnan and D. V. Gaitonde, A pressure decomposition framework for aeroacoustic analysis of turbulent jets, European Journal of Mechanics - B/Fluids **81**, 41 (2020).
[73] S. W. Rienstra, Fundamentals of duct acoustics, Von Karman Institute Lecture Notes (2015).
[74] J. Bruggeman, *Flow induced pulsations in pipe systems*, Ph.D. thesis, Department of Applied Physics (1987).
[75] P. Bradshaw, A note on poisson's equation for pressure in a turbulent flow, Physics of Fluids **24**, 777 (1981).
[76] A. M. Naguib and M. M. Koochesfahani, On wall-pressure sources associated with the unsteady separation in a vortex-ring/wall interaction, Physics of Fluids **16**, 2613 (2004).
[77] N. Curle, The influence of solid boundaries upon aerodynamic sound, Proceedings of the Royal Society of London. Series A. Mathematical and Physical Sciences **231**, 505 (1955).
[78] J. Larsson, L. Davidson, M. Olsson, and L. Eriksson, Aeroacoustic investigation of an open cavity at low mach number, AIAA journal **42**, 2462 (2004).
[79] G. Lam, R. Leung, and S. Tang, Aeroacoustics of t-junction merging flow, The Journal of the Acoustical Society of America **133**, 697 (2013).
[80] Y. P. Tang and D. Rockwell, Instantaneous pressure fields at a corner associated with vortex impingement, Journal of Fluid Mechanics **126**, 187 (1983).
[81] G. Haller and G. Yuan, Lagrangian coherent structures and mixing in two-dimensional turbulence, Physica D: Nonlinear Phenomena **147**, 352 (2000).
[82] M. Green, C. Rowley, and G. Haller, Detection of lagrangian coherent structures in 3d turbulence, Journal of Fluid Mechanics **18547**, 20 (2006).
[83] D. Rockwell and E. Naudascher, Self-sustained oscillations of impinging free shear layers, Annual Review of Fluid Mechanics **11**, 67 (1979).
[84] M. S. Mathias and M. A. F. Medeiros, The effect of incoming boundary layer thickness and mach number on linear and nonlinear rossiter modes in open cavity flows, Theoretical and Computational Fluid Dynamics **35**, 495–513 (2021).
[85] M. S. Howe, *Acoustics of fluid-structure interactions* (Cambridge University Press, 1998).
[86] M. S. Howe, *Theory of Vortex Sound*, Cambridge Texts in Applied Mathematics (Cambridge University Press, 2003).
[87] T. G. Bagwell, CFD simulation of flow tones from grazing flow past a deep cavity (2006) pp. 105–114.
[88] N. Forestier, L. Jacquin, and P. Geffroy, The mixing layer over a deep cavity at high-subsonic speed, Journal of Fluid

791 Mechanics **475**, 101 (2003).